



D4.5 - NUMERICAL INVESTIGATION OF SPOILER NOISE GENERATION AND MITIGATION

Document authors Owen Parnis David Angland Matteo Montecchia	Name (organization) University of Southampton University of Southampton CERFACS
Document contributors Etienne Charles	Name (organization) CERFACS

Abstract

In this deliverable, a numerical investigation of the acoustic sources of a spoiler is performed in order to understand the noise generation mechanisms and to give an insight into how they may be mitigated. In order to validate the numerical studies, a simple case involving a spoiler mounted on a flat plate is investigated at 30° in a wind tunnel test campaign. An experimental database consisting of aerodynamic loads, microphone measurements, on-surface pressure distributions, hot wire anemometry, and particle image velocimetry was produced in order to perform numerical simulation validation.

Numerical simulations, performed using a Lattice Boltzmann solver ProLB, are validated against these experimental data. While the geometry is relatively simple, this is still a challenging case to accurately predict numerically, particularly the boundary layer separation bubble that occurs upstream of the spoiler. The flow is characterized by an arch-type broadband wake without any coherent vortex shedding. There is a horseshoe vortex that originates upstream of the spoiler and wraps around both sides of the spoiler. There are also ground edge vortices, rotating in the opposite sense to, and inboard of, the horseshoe vortex on each side. The acoustic source associated with the ground edge vortices and the spoiler side-edges were the dominant acoustic sources in this configuration, particularly as the frequency increased.

After the validation of the numerical methodology, both groups (UoS and CERFACS) performed numerical simulations in order to determine the effect of different configuration. Reducing the spoiler angle to 10° weaken the horseshoe vortex. Also, the edge vortices stayed attached to the spoiler side edges for longer than at higher deflection angles. There was a strong broadband hump associated with flow through the spoiler gap at the hinge line. In terms of spoiler noise mitigation, this gap noise was identified as a potential source to be removed relatively easily.


Increasing the deflection angle to 90° showed the separation point moved upstream of the spoiler. This resulted in a much stronger horseshoe vortex. The main acoustic source was as it rolled up around the edges of the spoiler. The results showed that the exact dominant mechanism was dependant on the deflection angle. Again, for this case, the hinge gap was a source of noise. Yaw caused asymmetry and in general produced a noise increase over most frequencies. In terms of noise mitigation, the yaw angle should be minimised.

Keywords

Spoilers, wind tunnel tests, CFD simulations, aeroacoustics

1. Information Table

Project information	
PROJECT ID	860538
PROJECT FULL TITLE	INnoVative dEsign of iNstalled airframe componenTs for aircraft nOise Reduction
PROJECT ACRONYM	INVENTOR
FUNDING SCHEME	RIA – Research and Innovation Action
START DATE OF THE PROJECT	1st May 2020
DURATION	54 months
CALL IDENTIFIER	H2020-MG-2018-2019-2020

Deliverable information	
DELIVERABLE No AND TITLE	D4.5 Numerical investigation of spoiler noise generation and mitigation
TYPE OF DELIVERABLE1	Report
DISSEMINATION LEVEL2	PU
BENEFICIARY NUMBER AND NAME	7-SoU, 6-CERFACS
AUTHORS	Owen Parnis, David Angland, University of Southampton Matteo Montecchia, CERFACS
CONTRIBUTORS	Etienne Charles, CERFACS
WORK PACKAGE No	WP4
WORK PACKAGE LEADER WP LEADER VALIDATION DATE	Michael Pott-Pollenske, 08.09.2024
COORDINATOR VALIDATION DATE	Eric Manoha, 13.09.2024
Coordinator signature	

Use one of the following codes: R=Document, report (excluding the periodic and final reports)

DEM=Demonstrator, pilot, prototype, plan designs

DEC=Websites, patents filing, press & media actions, videos, etc.

OTHER=Software, technical diagram, etc.

ORDP : Open Research Data Pilot

Use one of the following codes: PU=Public, fully open, e.g. web

CO=Confidential, restricted under conditions set out in Model Grant Agreement

CI=Classified, information as referred to in Commission Decision 2001/844/EC.

2. Table of Contents

1. Information Table	3
2. Table of Contents	4
3. Introduction	5
4. Experimental Methodology.....	5
5. LBM Numerical Setup	8
5.1 Configuration Summary	8
5.2 Southampton Numerical Setup	9
5.2.1 Simulation Setup	9
5.2.2 Simulation Configuration and Mesh Description	10
5.2.3 Simulation Output Setup	13
5.3 CERFACS Numerical Setup	13
6. Numerical Validation	15
6.1 Forces and On-Surface Pressures.....	15
6.2 Hotwire Anemometry	16
6.3 Particle Image Velocimetry.....	21
6.4 Acoustic Measurements	23
6.5 Best Practice.....	25
7. Numerical Results	27
7.1 10 deg. Case.....	27
7.2 90 deg. Case.....	33
7.3 Extended Chord	37
7.4 Yawed Case.....	38
7.5 Side-by-Side (Simultaneous Deflection)	42
7.6 Side-by-Side (Spilt Angles)	42
8. Summary	45
9. References.....	47

3. Introduction

This deliverable is an output of Task 4.4. This task is dedicated to the exploration of spoiler noise on a purely numerical basis. A generic small-scale model was built and measured in a wind tunnel to validate a Lattice Boltzmann solver. The output is a validation of the solver for spoiler noise. The validated numerical methodology is then used to assess the sensitivity of spoiler noise to various different configurations detailed below.

During a steep descent, spoilers can be deployed as a noise abatement procedure to reduce the approach velocity of an aircraft. Once deployed, the spoiler induces changes in the circulation of the high-lift wing, leading to changes in the slat and flap noise sources and introducing its own additional source (Dobrzynski, 2008). In order to separate these effects and fully understand the flow topology leading to the noise generation of a deployed spoiler, studies were conducted on a spoiler mounted to a flat plate. This eliminates external sources such as effects induced by additional devices such as the slat and flap and additional lifting wing circulation effects.

The report aims to define the noise sources generated by an inclined wall-mounted flat plate spoiler of finite thickness as a function of a change of deflection angle and spoiler configuration. The noise source generation will be related to each configuration's flow topology generated by the deflected spoiler.

The deflected spoiler's flow topology and noise sources will be analysed numerically using a Lattice Boltzmann solver, ProLB. The numerical simulations will be validated against experimental results obtained for a deflection angle of 30° . By selecting a deflection angle of 30° , this study aims to represent the typical deflection angle at which spoilers are deployed during the approach phase of flight.

A comparison of how the noise sources vary with deflection angle and spoiler configuration will be assessed. Sound mitigation improvements to reduce spoiler noise will be provided from the results obtained.

4. Experimental Methodology

The experiments used for numerical validation were conducted at the anechoic wind tunnel facility at the University of Southampton (SotonAWT). The tunnel is an open jet, closed return, wind tunnel with a nozzle cross-section of 0.75 m by 1 m. The wind tunnel's axis of origin, O is located at the centre of the exit of the nozzle, with the positive x axis denoting the downstream direction, the positive y axis the span direction, and the positive z axis indicating the vertical direction as illustrated in Figure 4.1. In an empty test section, the maximum freestream velocity of the tunnel reaches approximately 80 m/s. The anechoic chamber is fitted with acoustic wedges and is anechoic down to a frequency of 250 Hz.

The finite span, flat plate spoiler model was constructed from a thin steel plate with a chord of $c = 106$ mm and a span $b = 247$ mm. The aspect ratio of the plate is equal to 2.3. The thickness of the plate is $t = 6$ mm. No edge rounding was performed on the flat plate's sharp edges. The spoiler was deflected in the direction of the incoming flow stream using two brackets mounted to the downstream face of the spoiler.



A schematic representation of the wall-mounted flat plate model is shown in Figure 4.1 with the deflection angle θ measured between the spoiler (defined as zero when the flat plate is aligned with the freestream velocity vector) and the base mounting plate. The experiments were conducted at a free stream velocity of 60 m/s, corresponding to Reynolds numbers of 4.47×10^5 , calculated based on the chord length of the spoiler plate. The model was securely mounted on a base plate attached to the lower lip of the wind tunnel nozzle, creating a three-quarters open test section. This configuration ensured quiescent flow underneath the base plate section. The model's origin was fixed at a specific location, with $x_{LE} = 647$ mm and $z_{LE} = -375$ mm measured with respect to the wind tunnel's origin.

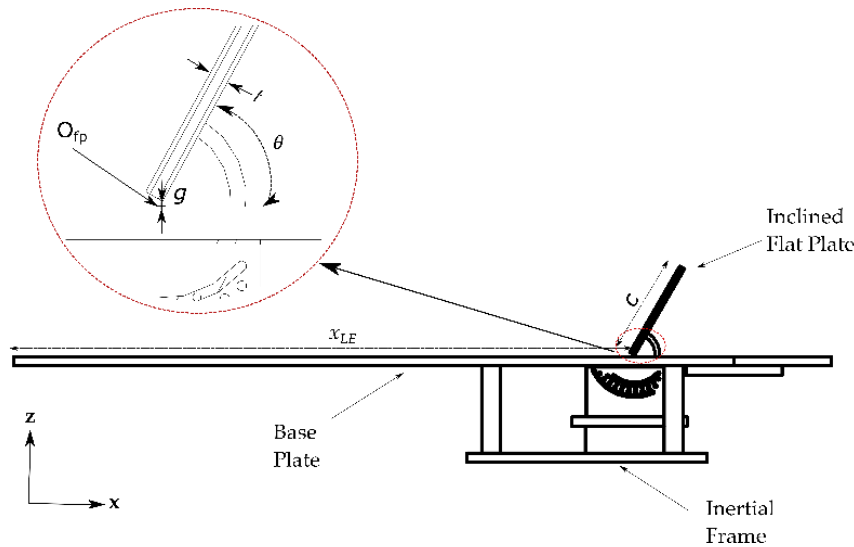


Figure 4.1: Schematic of the inclined wall-mounted flat plate spoiler geometry.

A small gap was designed between the leading edge of the downstream face of the flat plate and the base plate. This was implemented to ensure the complete transfer of all aerodynamic loads acting on the flat plate to the load cell. The gap size, denoted as g , between the leading edge and the base plate, varied with the deflection angle of the flat plate model, reaching a maximum gap ratio of $g/c = 0.032$. At the position of the spoiler's leading edge, the boundary layer thickness to gap ratio, represented as δ/g , which was equal to 9. The presence of the inclined flat plate introduces an adverse pressure gradient upstream of it, which varies with the deflection angle. This adverse pressure gradient leads to the thickening of the boundary layer upstream of the flat plate. Consequently, the gap becomes significantly immersed within the boundary layer, where the velocities are significantly lower than the freestream velocity.

Different experimental methodologies were used to validate the numerical simulations to generate an experimental data set of the flow characteristics surrounding the deflected spoiler. Aerodynamic loads and moments exerted on the model were measured using an ATI Delta 6-component transducer connected to the inertial frame of the model. The directions of the drag force, side force and lift force, as measured by the load cell, coincide with the wind tunnel axis defined. The drag and lift forces are aligned along the wind tunnel's x and z axes. The same definition can be applied to the moments, where the pitching moment acts along the y axis and is positive according to the right-hand rule. Force measurements were taken at a sampling rate of 1 kHz.

Acoustic measurements were conducted using a combination of far-field microphones and a phased microphone array. To acquire the far-field noise of the flat plate of a given deflection and velocity, 13 GRAS 1/4" 46BE microphones were used. The microphones were set up as shown in Figure 4.2(a). Seven overhead microphones were set up along $y = 0$ m (corresponding to the mid-span of the model) to capture the flyover arc for polar angles between 65° and 102° . Three additional microphones were set up in the same z plane but at an offset distance of $y = -123.5$ mm, corresponding to the half span of the plate. These microphones were set up to analyse any directivity along the edge of the flat plate. Finally, to measure the noise radiated to the side of the model, one microphone was placed in the far-field along the side of the model, directed towards the trailing edge of the inclined plate. Two further microphones were placed on the floor downstream of the trailing edge of the base plate.

Unsteady pressure measurements were done within the recirculation region downstream of the spoiler along the streamwise plane ($y = 0$ m) using two Kulite pressure transducers XCQ-093. Data acquisition was done at a frequency of 48 kHz for a total sampling time of 10 seconds.

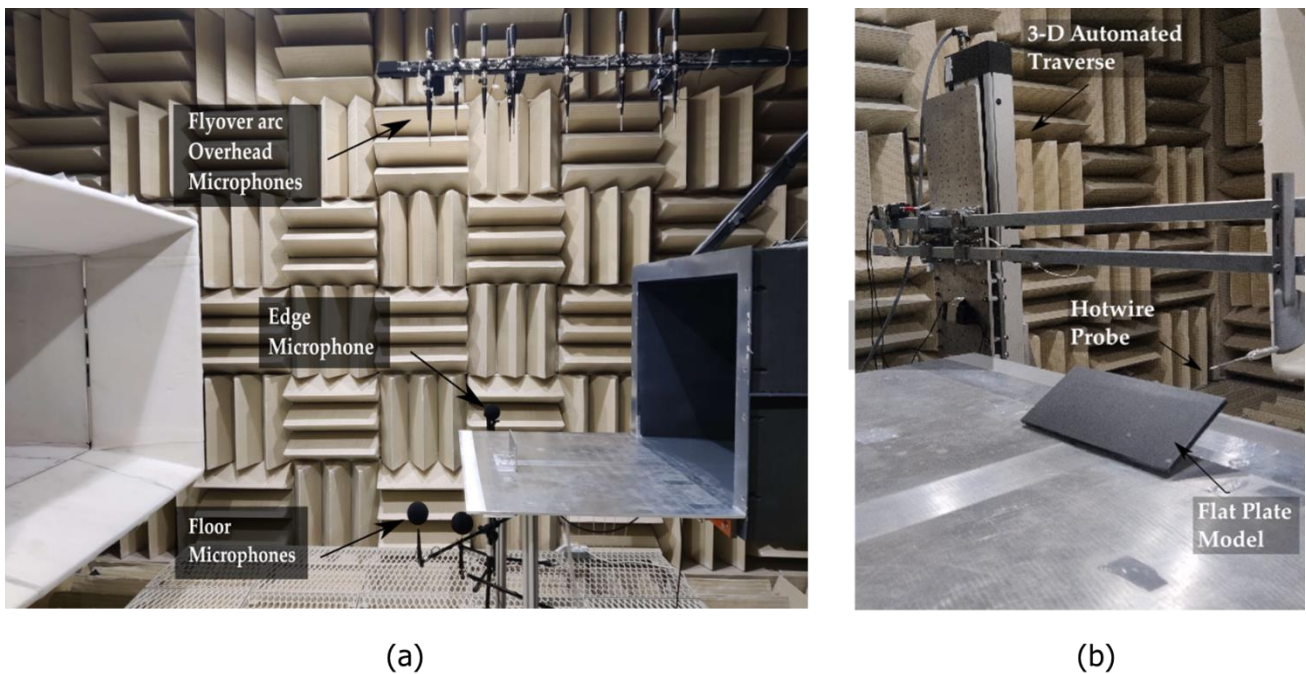


Figure 4.2: Experimental setup used in SotonAWT for different methodologies: (a) Far-field Acoustics; (b) Wake hotwire measurements.

Hot-wire measurements were conducted using a single-probe hot-wire sensor to analyse the turbulent wake downstream of the plate. The probe was mounted on a three-dimensional automated traverse system and connected to a DANTEC MiniCTA 54T30 anemometer. The data acquisition was performed using a National Instruments NI-4497 card at a frequency of 48 kHz, with a sampling time of 10 seconds.

The streamwise characterisation and wake growth of the wake downstream of the inclined spoiler plate were determined using Particle Image Velocimetry (PIV). Two-dimensional time-averaged PIV analysis was performed utilising a Mono-PIV-based technique. Velocity vectors in the streamwise and normal (to the incoming flow) directions were measured along the symmetry axis of the model ($y = 0$ m). A laser sheet was generated above the model and illuminated the near downstream wake of

the mounted plate. Images were captured using a 25 MP LaVision Imager CX series camera with a maximum resolution of 5296 x 4584 pixels and a frame rate of up to 30.4 Hz.

5. LBM Numerical Setup

5.1 Configuration Summary

To understand the impact of noise generation on wall-mounted deflected spoilers and how such impact can be reduced, a parametric study was conducted for different spoiler deflection angles and geometries. Four different spoiler configurations were assessed: the baseline spoiler configuration, the extended chord configuration, the side-by-side configuration and the yawed configuration. The different configurations are shown in Figure 5.1.

The baseline configuration is a single wall-mounted flat plate spoiler, which is fixed parallel to the velocity inlet boundary condition at a yaw angle, $\psi = 0^\circ$, with respect to the default z axis. To assess the impact of the deflection angle on the noise generated by a wall-mounted spoiler, three deflection angles were studied: 10° , 30° and 90° . The case in which the spoiler was deflected at 30° was selected as the validation case. It is the most representative case compared to the typical deployed spoiler angle used in flight.

The impact of the noise generated by a spoiler due to geometric changes will be assessed in terms of changes in the chord length, span length and changes in the yaw angle with incoming freestream velocity. For direct comparison with the baseline case, these configurations will be analysed with the spoiler deflected at an angle of 30° .

Configuration	Deflection Angle	Organisation	Freestream Velocity
Baseline	10°	UoS	60 m/s
Baseline	30°	UoS/ CERFACS	60 m/s
Baseline	90°	UoS	60 m/s
Extended Chord	30°	CERFACS	60 m/s
Yaw 10°	30°	UoS	60 m/s
Side-by-side (simultaneous deflection)	30°	CERFACS	60m/s
Side-by-Side (split angles)	$40^\circ - 50^\circ$	CERFACS	60 m/s

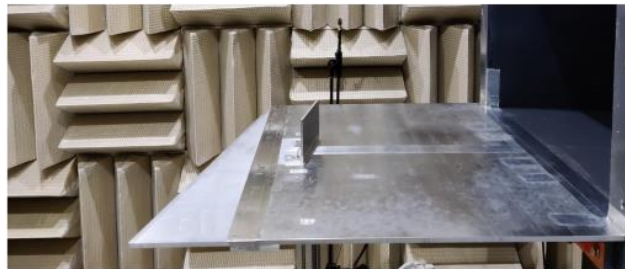
Table 1: Summary of configurations tested.



Config 1 & 2: Baseline /Extended Chord



Config 3: Extended Span



Config 4: Swept

Figure 5.1: Description of the spoiler configurations analysed: (a) Baseline and Extended Chord Configuration, (b) Side-by-Side Configuration, (c) Yawed Configuration.

The extended chord configuration is similar to the baseline configuration in which the chord of the spoiler is $1.5c$ of the baseline. The side-by-side spoiler configuration consists of two adjacent spoiler deflected at a yaw angle of 0° . A small gap of 1 mm was designed between the two spoiler plates to allow for independent deflection. The ability to independently deflect the different spoilers enables both simultaneous and independent deflection studies, in which both spoilers are deflected at different deflection angles leading to a geometric discontinuity to form along the trailing edges of the individual plates. The cases were studied at a freestream velocity of 60 m/s equivalent to $Re = 4.47 \times 10^5$. The analysis of the different configuration was a joint effort between the University of Southampton and Cerfacs. Table 1 summarises the different configurations tested at the corresponding spoiler deflection angles.

5.2 Southampton Numerical Setup

5.2.1 Simulation Setup

A schematic of the simulation domain is shown in Figure 5.2. The size of the external fluid domain is equal to $8L_{\text{nozzle}}$ and $9L_{\text{nozzle}}$, where L_{nozzle} is equivalent to the width of the nozzle outlet equal to 1 m. The width of the fluid domain is equal to $8L_{\text{nozzle}}$. A pressure outlet boundary condition was set at the fluid domain with the pressure equal to the ambient pressure, p_{amb} . To reduce far-field reflections of the propagating acoustic waves from the edge of the computational fluid domain, a buffer region with a thickness of 2 m was set up. The thickness was selected to allow enough mesh points within the sponge zone to allow for sufficient damping.

To achieve similarity with the open jet flow exiting the nozzle of the wind tunnel, the simulations were done using a straight wind tunnel duct. This is similar to the setup performed in Task 3.2. The duct length is equal to 1.8 m, and the geometry of the nozzle exit is equal to that of the open jet wind tunnel. A velocity inlet boundary condition set to the freestream velocity, U_∞ was defined at the start of the straight duct. An inlet damping layer was used to reduce acoustic wave reflections along the inlet boundary. The thickness of the inlet layer is equal to 0.5 m. The geometric model was fixed to

the lower lip of the nozzle of the straight wind tunnel duct. The origin of the coordinate system was set at the centre of the nozzle exit, as shown in Figure 5.2. The leading edge of the spoiler is at a distance of 0.647 m from the nozzle exit. The incoming flow is uniform with a freestream velocity of $U_\infty = 60$ m/s, temperature of $T = 288$ K and density of $\rho = 1.23$ kg/m³. The equivalent speed of sound was equal to 340.18 m/s, resulting in a reference Mach Number of $Ma = 0.18$.

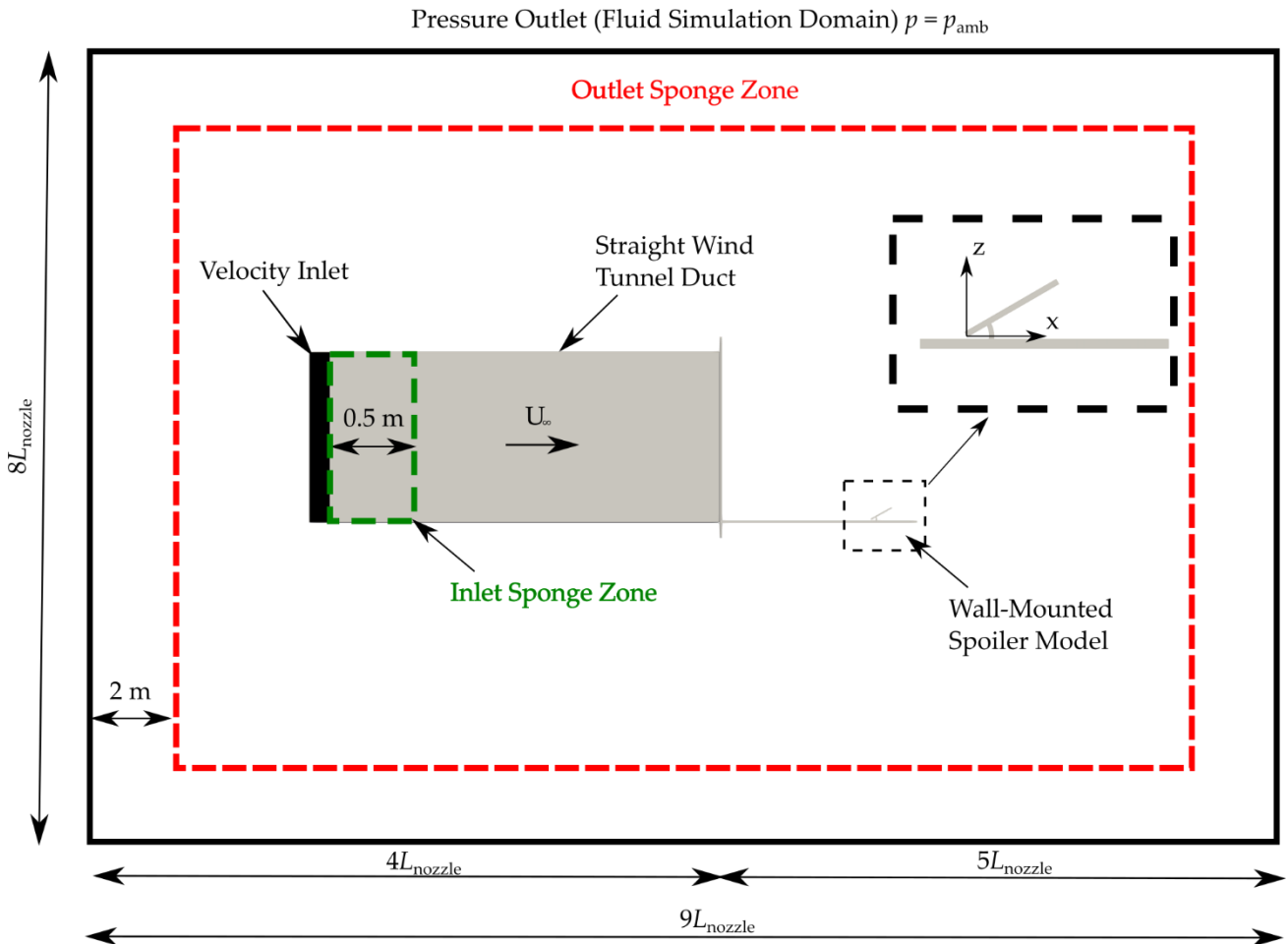


Figure 5.2: Schematic of the Simulation Domain

5.2.2 Simulation Configuration and Mesh Description

ProLB™ utilises a Lattice Boltzmann Method (LBM) kernel using the D3Q19 lattice scheme having a Dual Relaxation Time (DRT) collision operator as described by Leveque et. al. (2018). This scheme defines a more robust and accurate scheme when compared to the traditional collision model defined by the BGK collision methods. Meshes are generated using a fully parallel octree mesh generator embedded in the ProLB solver to refine cubic meshes in an octree manner. Unsteady simulations for turbulent flow are done using wall-modelled large eddy simulations with a subgrid-scale model based on the shear-improved Smagorinsky model (SISM). The wall law is modelled using a log law with an adverse pressure gradient, as proposed by Afzal (1996). The use of wall functions improve the computational efficiency by reducing mesh sizes when compared to a wall-resolved approach.

The minimum on-surface mesh size was set to $\Delta x = 0.25$ mm. Subsequent refinement was done in the near-field downstream wake of the deflected spoiler up to a distance of $5c$ (shown in Figure 5.4), resulting in a total mesh size of 109 million cells. This setup led to a minimum numerical time step,

denoted as Δt , equal to 4.24×10^{-7} s. The mesh refinement for all the components is shown in Figure 5.3. Two refinement regions (RF) for direct propagation were set up to allow for a controlled mesh size growth up to the direct propagation receivers. The mesh levels were selected to ensure that at least eight mesh points per wavelength were used in regions of direct noise propagation. This allowed for a maximum resolvable frequency of 10.6 kHz.

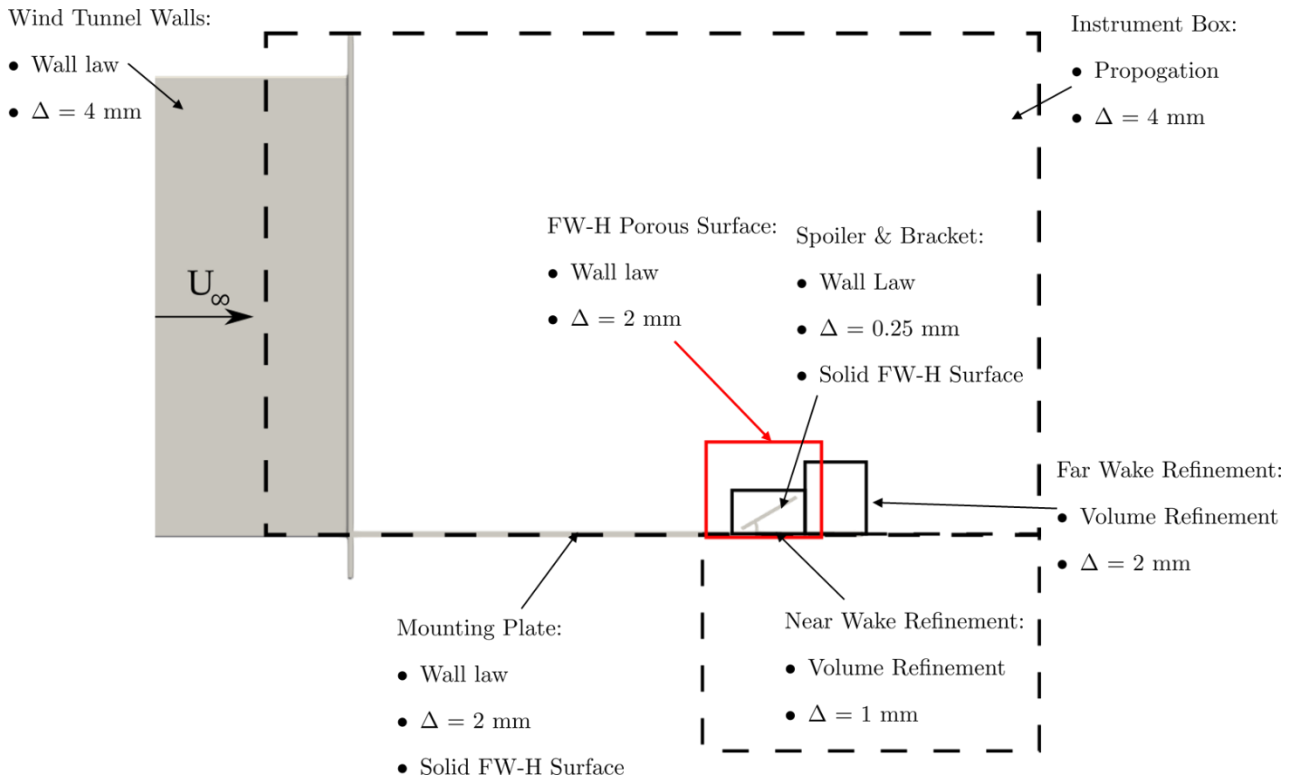


Figure 5.3: Simulation setup.

Acoustic analysis was done by analysing a Ffowcs Williams Hawkings (FW-H) solver. Various integration surfaces were placed surrounding the model. A combination of porous and solid FW-H surfaces was used. The porous surface enclosed the spoiler and the adjacent endplate region. The porous surface was set up to be big enough such that the hydrodynamic turbulence from the separated region upstream of the spoiler does not pass through the side faces of the rectangular enclosure. A refinement of $RF = 4$, equivalent to a mesh size of $\Delta_{FWH} = 2$ mm, was defined, allowing for a maximum resolvable frequency of 21.2 kHz for acoustic pressure fluctuations. The solid FW-H surface was defined directly from the individual geometric surfaces used in the model. Hence, three sets of solid FW-H surfaces were analysed: (1) spoiler plate and brackets, (2) endplate and trailing edge, and (3) all the solid surfaces. This was done so that the contribution of each geometric body in the model could be assessed independently. The mesh refinement of each surface is provided in Figure 5.3.

As described in section 2, a hinge gap was modelled between the leading edge of the spoiler and the endplate. To allow for similarity the same hinge gap was recreated in the numerical setup. A mesh refinement of $\Delta = 0.25$ mm was used, shown in Figure 5.4.

Additionally, upstream mesh refinement was done along the central region of the endplate upstream of the deflected spoiler plate to ensure that the incoming developing boundary layer is characterised correctly and that the upstream y^+ values are between 30 and 300 for the wall log law to be valid.

Due to limitations of the wall model, a limit to the achievable refinement was observed before the formation of upstream premature separation resulting in non-physical vortex structures to form along the endplate. To ensure that the boundary layer develops correctly, a higher y^+ of 260 was used having a mesh size of $\Delta = 2$ mm. This ensures that the cell size is within the log region of the law of the wall.

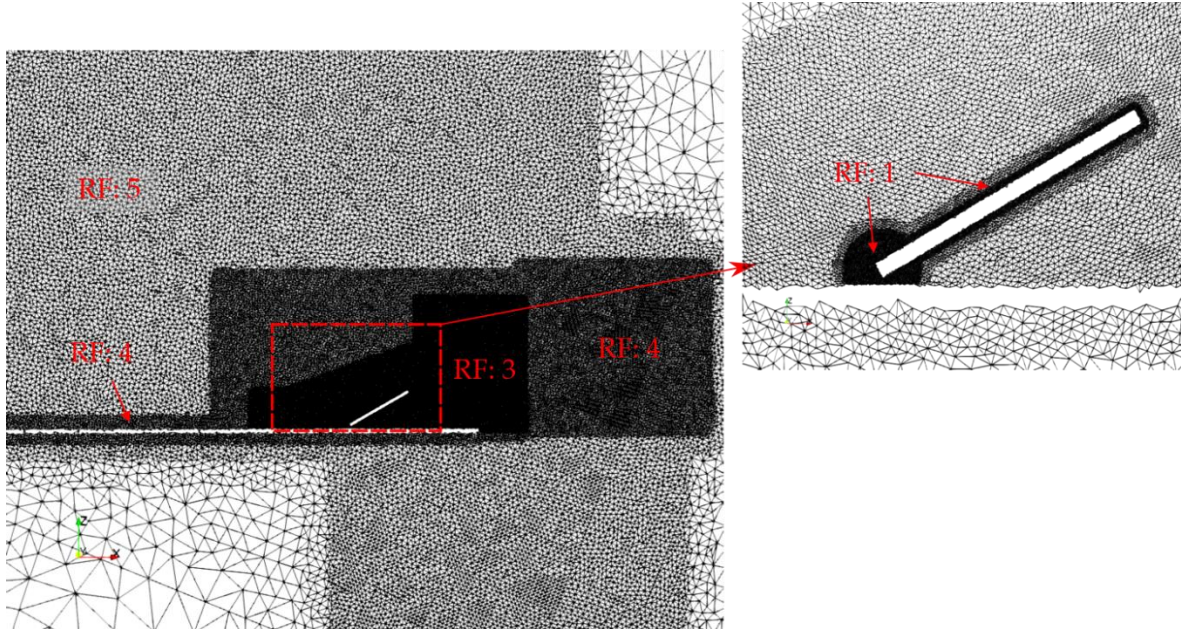


Figure 5.4: Mesh refinement regions (RF) along the spoiler.

Table 2 summarises the setup parameters which were used in the numerical simulations.

Feature	Condition
Model Parameters	
Turbulence Model	Wall Modelled LES with Shear Improved Smagorinsky Model
Thermal	OFF
Physical Parameters	
Reference Pressure (Pa)	1.0127×10^5
Reference Density (kg/m^3)	1.23
Reference Velocity (m/s)	60
Molecular weight (g/mol)	28.97
Gamma	1.4
Kinematic viscosity (m^2/s)	1.49×10^{-5}
Numerical Parameters	
Minimal mesh size: Δ (mm)	0.25
Simulated Time (s)	0.308

Table 2: Summary of the setup parameters used in the numerical simulations

5.2.3 Simulation Output Setup

To order to allow different simulations from the two different groups to be compared, a fixed number of outputs from each simulation was defined. As part of this several different point recordings were done at different locations in the fluid domain. The description and the location of the different point recordings are provided in Figure 5.5. Output results included on surface pressure measurements, turbulence wake mapping, noise source location using beamforming, aerodynamic loads and far-field acoustics.

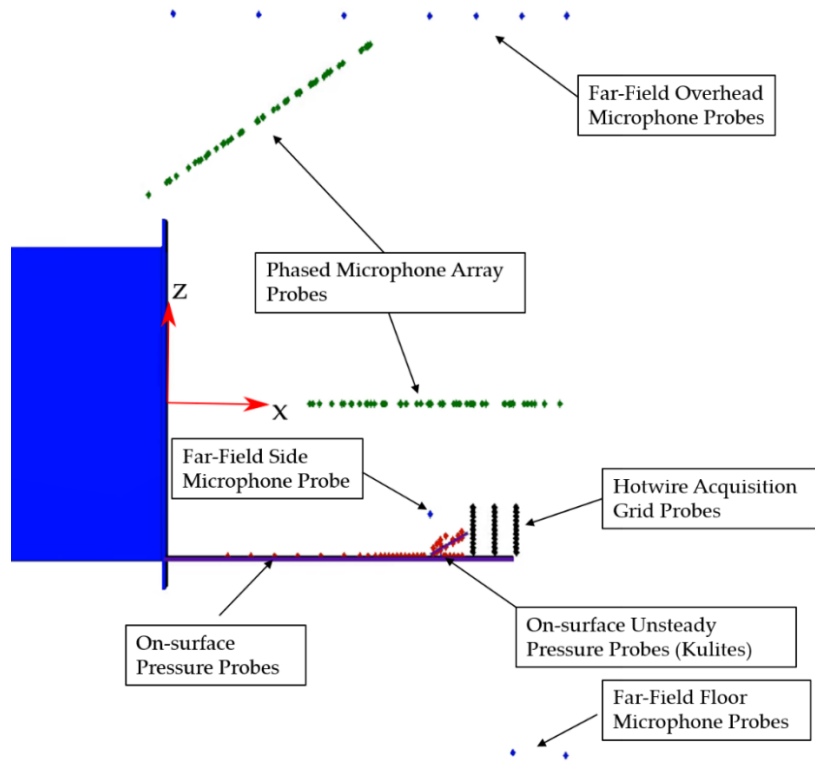


Figure 5.5: Simulation output probes

5.3 CERFACS Numerical Setup

The geometry employed in CERFACS simulations is the same as the one adopted by UoS. Similar boundary conditions are applied, following the UoS approach, except for the wind tunnel inlet and outlet. In these specific locations, LODI boundary conditions are applied, specifying freestream velocity and ambient pressure, respectively.

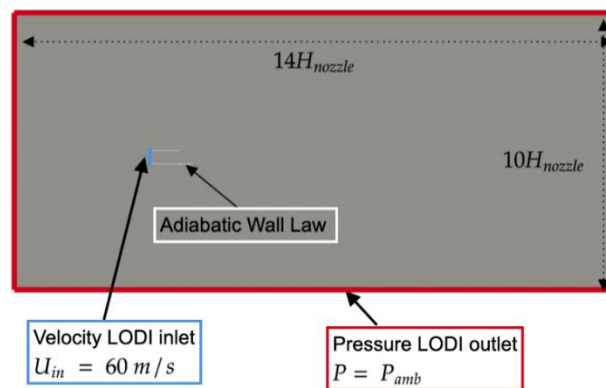


Figure 5.6: Scheme of the setup with boundary conditions.

The solver adopted for the present study is ProLB 2.8 with a HRRD3Q19 collision scheme, a MUSCL scheme is enabled for the energy equation and a centered scheme for the gradients at the walls is used. The Sutherland viscosity model is utilised, and the mesh structure, depicted in Figure 5.7, remains the same across all cases. The mesh size is designed to capture the highest frequency acoustic waves, corresponding to a Strouhal number of 10. This results in minimum cell sizes of 2.2×10^{-4} m and 2.7×10^{-4} m for the baseline and other cases, respectively. Figure 5.7 (right) illustrates that the finest refinement zones are strategically placed on the spoiler and at the endplate-spoiler joint, with a second refinement level (RF2) applied to the endplate's boundary layer.

To facilitate a laminar-to-turbulent transition, tripping elements are positioned at the wind tunnel exit. More details will be provided in the following section.

All simulations ran for 4.5 convective times, defined as the ratio of the nozzle length and velocity, for a total duration of about 0.05 seconds. Acoustic acquisition occurs during the last convective time.

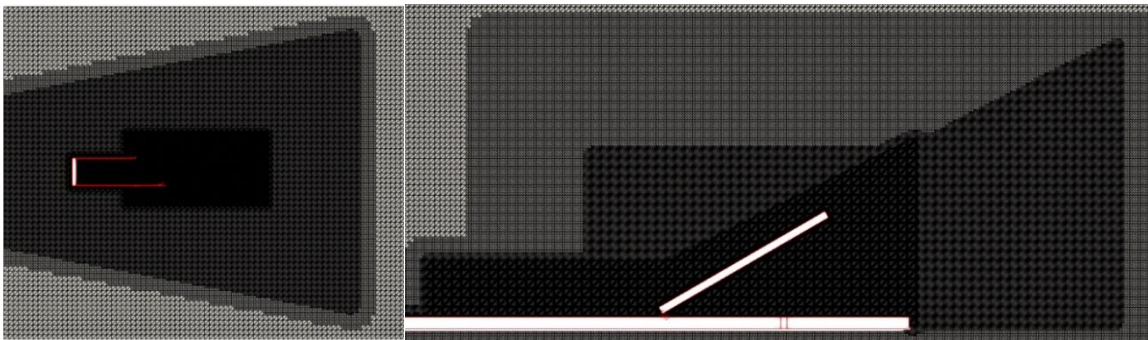


Figure 5.7: View of the entire mesh (left) and close-up towards the spoiler (right)

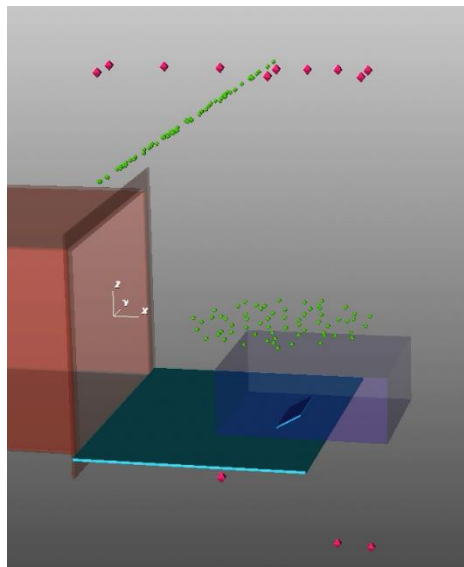


Figure 5.8: Microphones arrays.

Various techniques have been employed for acoustic data acquisition. Phased arrays of microphones, as depicted in Figure 5.8, are positioned at 0° and 45° , on mesh level RD6, corresponding to a maximum Strouhal number ranging between 3 and 5. Direct noise acquisition is carried out at the same mesh level. Additionally, a porous FWH surface is located at mesh level RD5, denoted by the purple box in Figure 5.8, resulting in a maximum Strouhal number of approximately 10. Acoustics at Strouhal numbers greater than 10 is captured by a solid FWH surface on a mesh level RF4, positioned

on the spoiler surfaces and the wind tunnel endplate. The Antares post-treatment library is utilised to propagate porous FWH surface data to the microphones' positions.

6. Numerical Validation

This section will present the numerical validation of the numerical simulation against the experimental data for a spoiler deflected at an angle of 30° . Validation is conducted to ensure that the aerodynamic characteristics obtained from the numerical simulation are consistent with the experimental results. It is one of the key outputs of this task. The validation compares the numerical results with the corresponding experimental results, including the aerodynamic loads, far-field noise spectra, on-surface unsteady pressures, and wake characteristic comparisons using PIV and hotwire anemometry.

6.1 Forces and On-Surface Pressures

A comparison of the simulated aerodynamic load coefficients with the experimental data is shown in Table 3. Compared to the experimental results, for a spoiler deflected at 30° , the drag coefficient and the lift coefficient from the numerical simulations are observed to over predict the experimental values by $\Delta C_D = +0.02$ and $\Delta C_L = -0.051$, respectively. The reference area used is the planform area of the spoiler.

Methodology	C_D	C_L
Experiment	0.221 ± 0.014	-0.333 ± 0.026
ProLB	0.241	-0.384

Table 3: Aerodynamic load coefficients compared to experimental results for a wall-mounted spoiler deflected at $\theta = 30^\circ$ at $Re = 4.47 \times 10^5$

The difference in the value of the aerodynamic loads between the experimental and numerical methodologies stems from the fact that the upstream characteristics, as simulated by ProLB, do not fully match those obtained experimentally as will be shown in the pressure measurements. Figure 6.1 depicts the on-surface mean pressure characteristics along the symmetry plane of the model.

The numerical simulations slightly underestimate the on-surface pressure up to a distance of $x/c = -2$. The main reason for such a difference is the difference in the incoming boundary layer profile. The first cell height on the flat plate was tuned to give the best agreement, albeit still with some differences. As a result the pressure on the upstream face of the spoiler are not exactly the same as the experiments resulting in slight variations in the overall loads, ultimately resulting in a higher overall pressure along the upstream face when compared to what was observed experimentally. Downstream of the spoiler, it is observed that both the experiments and ProLB achieve the same base pressure along the downstream face of the spoiler and the downstream region of the endplate within the base re-circulation region of the wake. Hence, the component of the pressure drag numerically is observed to be slightly higher than that experimentally, resulting in a slight over prediction of the aerodynamic loads on the deflected spoiler plate.

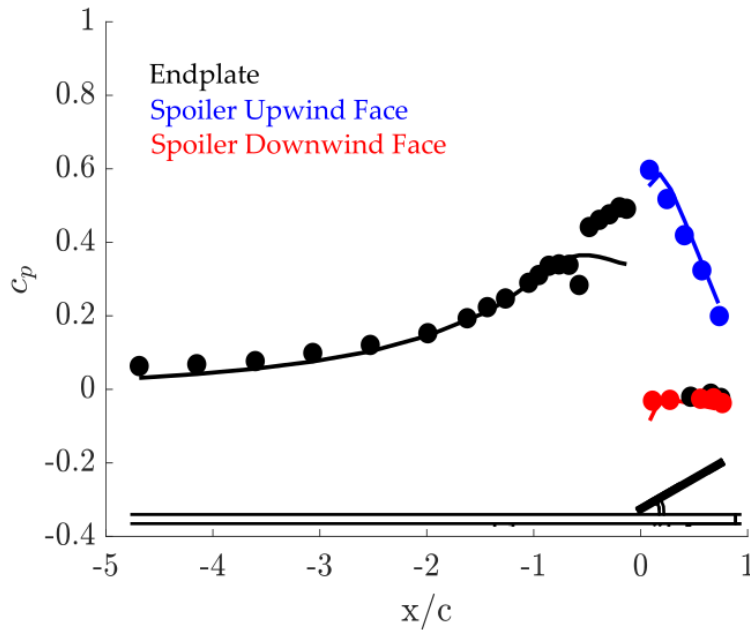


Figure 6.1: On-surface pressure comparison between experimental (o) results and numerical results (-) comparison along the endplate (black), upstream face of the spoiler (blue) and downstream face of the spoiler (red).

6.2 Hotwire Anemometry

Validation of the wake characteristics and the turbulence fluctuations in the wake were done by comparing directly sampled data in ProLB with single probe hotwire experimental data. The wake was characterised using velocity mapping of z - y planes at three different locations downstream of the inclined flat plate spoiler and by spectral analysis of the turbulent perturbations along different locations in the wake. The acquisition plane locations with respect to the location of the inclined flat plate spoiler are shown in Figure 6.2. The location of each acquisition plane is P1: $x/c = 1$; P2: $x/c = 1.5$ and P3: $x/c = 2$.

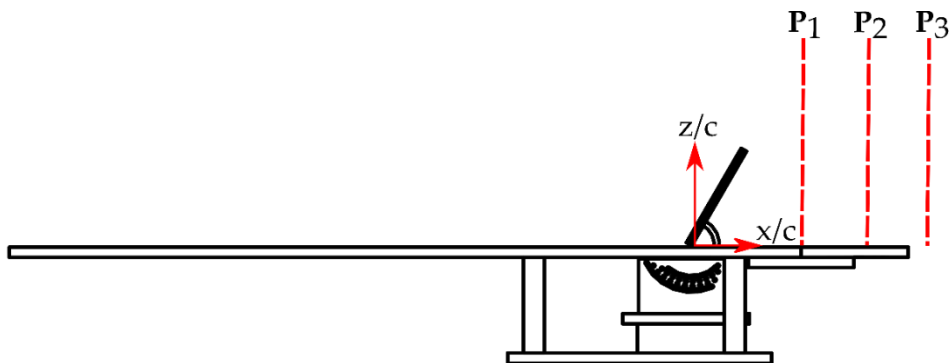


Figure 6.2: Location of the hotwire acquisition planes downstream of the spoiler. The location of each plane is as follows: P1: $x/c = 1$; P2: $x/c = 1.5$, P3: $x/c = 2$ from the leading edge of the spoiler.

Due to the physical proximity of plane P1 to the trailing edge of the spoiler and the influence of reversed flow on the probe, results from P1 are not analysed. Along this plane, the probe is immersed in the bluff body recirculation region, leading to strong cross-wind tangential components and reversed flow, which a single probe hot wire will not accurately measure.

At any of the three measuring locations downstream of the inclined flat plate spoiler, the velocity measurements were collected at a number of locations lying on the measuring plane shown in Figure 6.3. The height and span of the acquisition plane are normalised with respect to the chord and span of the flat plate spoiler, respectively. The ensemble of these measurement locations formed a grid of acquisition points spanning the whole span of the flat plate and extended beyond the edges of the flat plate allowing for downstream wake growth. The spatial resolution of the grid array used to map the wake planes was selected to obtain a fine spatial resolution in high turbulent intensity regions in the wake. These regions span the base region and the trailing and side edges of the inclined plate. The remaining spatial resolution was acquired using a much coarser zonal grid. A total of 231 acquisition points were acquired.

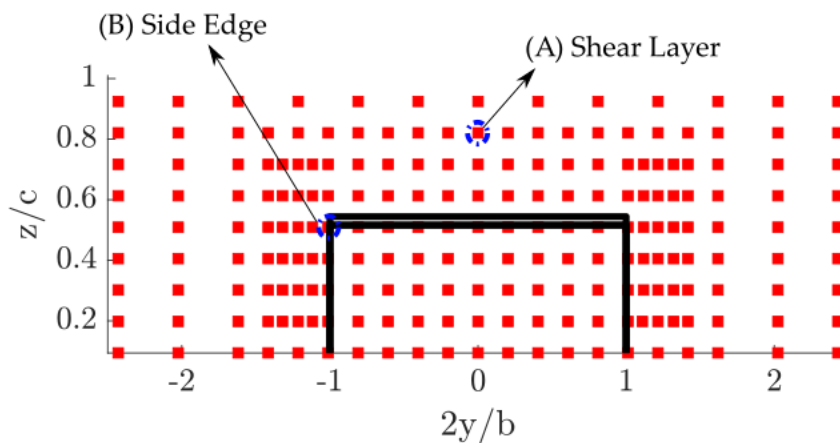


Figure 6.3: Acquisition grid utilised for mapping the flat plate spoiler wake. The two locations highlighted relate to the locations where the turbulent spectra were compared: (A) Probe location along the shear layer generated; (B) probe location along the side edge of the spoiler.

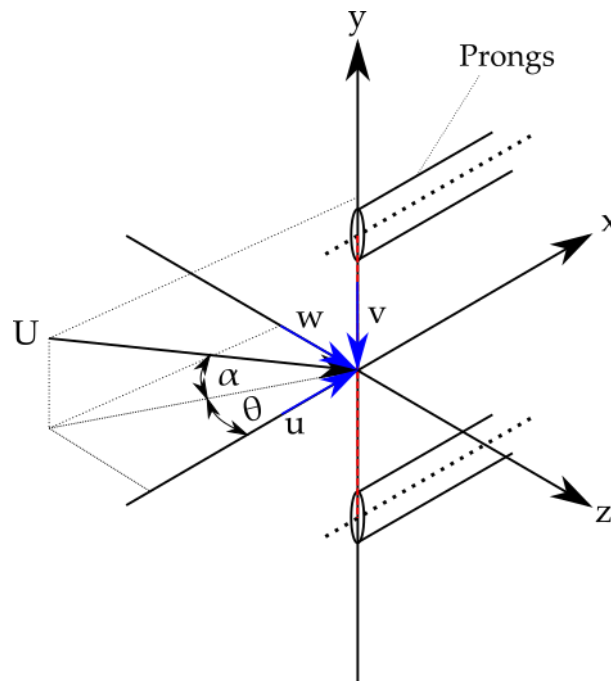


Figure 6.4: The velocity components and angle notation of an instantaneous velocity vector being acquired by a single hot wire probe placed with the probe stem parallel to the mean flow direction.

The numerical instantaneous velocity was calculated at different probe locations by calculating the three-dimensional effective cooling velocity, \bar{U}_{eff} as shown in Equation 1 (Jorgensen, 1971). The effective cooling velocity considers the directional sensitivity of the hot wire probe in terms of pitch and yaw angle effects of the instantaneous velocity component as defined in the coordinate system established in Figure 6.4. Hence, the numerical three-dimensional instantaneous velocity vector as established by a probe in the flow would be analysed the same way as a three-dimensional flow experienced by a single hot wire probe parallel to freestream (C Tropea, 2007) (Bruun, 1995).

$$\bar{U}_{eff}^2 = U_N^2 + h^2 U_B^2 + k^2 U_T^2 \quad \text{Eq.1}$$

Where U_N is the normal velocity component to the probe along the x -axis, U_B is the binormal velocity component to the probe along the z -axis, U_T is the tangential velocity along the length of the wire along the y -axis, h is the pitch correction factor for the binormal velocity vector introduced to compensate for the acceleration of the flow over the wire due to the presence of the side prongs and k is the yaw correction factor along the tangential velocity to correct for the increase in the heat transfer rates parallel to the wire due to the tangential component of the incoming flow. The correction factor values depend on the hotwire probe type, freestream velocity and yaw angle. For the analysis presented, a value of $k = 0.2$ and $h = 1.1$ are used for a miniature single probe hot wire (Jorgenson, 2002).

The turbulence fluctuations were assessed by analysing the power spectral density of the time series of the instantaneous velocity perturbation component as measured by the hot wire probe. The reference velocity was taken as equal to the freestream velocity, $U_\infty = 60$ m/s. Two locations were selected for validation, highlighted in Figure 6.3. Point A defines a point within the free shear layer convecting downstream from the trailing edge, and point B defines a point downstream behind the side edge of the spoiler. Analysis of the spectra produced by these two spoiler locations identifies the presence of any coherent vortex shedding, if any, present downstream of the spoiler, leading to a parasitic tonal noise radiation to the far field. The results were conducted for plane P2 at $x/c = 1.5$ and P2 $x/c = 2$ from the leading edge of the spoiler. The results shown in Figure 6.5, from the two methodologies at the two different acquisition planes, show broadband spectra without any coherent vortex shedding present in the wake. As the spoiler is placed in proximity to the endplate, the formation of a shear layer of opposite sign vorticity is inhibited. Hence, coherent von-Karman-type vortex shedding downstream of the spoiler plate is suppressed. Similarly, due to the large aspect ratio of the spoiler plate, coherent shedding between the two free side edges is also suppressed due to the formation of non-coherent symmetric arch-type vortices downstream of the plate (H. Sakamoto, 1986), (H Sakamoto, 1983).

Higher turbulence perturbations are observed for the regions within the free shear layer at the trailing edge compared to those along the side edges of the spoiler. This is also highlighted in the normal velocity perturbations, u' , turbulence intensity plot provided in Figure 6.6 and Figure 6.7 for the planes P2 and P3, respectively.

When comparing the turbulent perturbation spectra obtained from both methodologies, along the free shear layer generated from the trailing edge of the spoiler Figure 6.5(A), excellent agreement was observed between the two spectra obtained for each methodology. The noise observed in the

numerical spectra stems from inadequate averaging since a shorter acquisition time results in a smaller sample size than the experimental results.

When comparing the perturbation spectra obtained along the side edge of the trailing edge shown in Figure 6.5(B), disagreement is observed at this location for frequencies larger than 1.2 kHz. Disagreement in the two spectra arises from the fact that at this probe location, especially for the signal at plane P2, the probe is still immersed in the bluff body recirculation region in the wake. As a result, the two-time signals obtained in both methodologies will not be the same due to the reverse flow component of the wake. In the experiments, the reverse flow will be acquired as shedding from the stem of the hotwire probe. At plane P2, better agreement is observed for a higher narrowband frequency range up to 5 kHz. This said the impact of the reverse flow region is still observed at high frequencies.

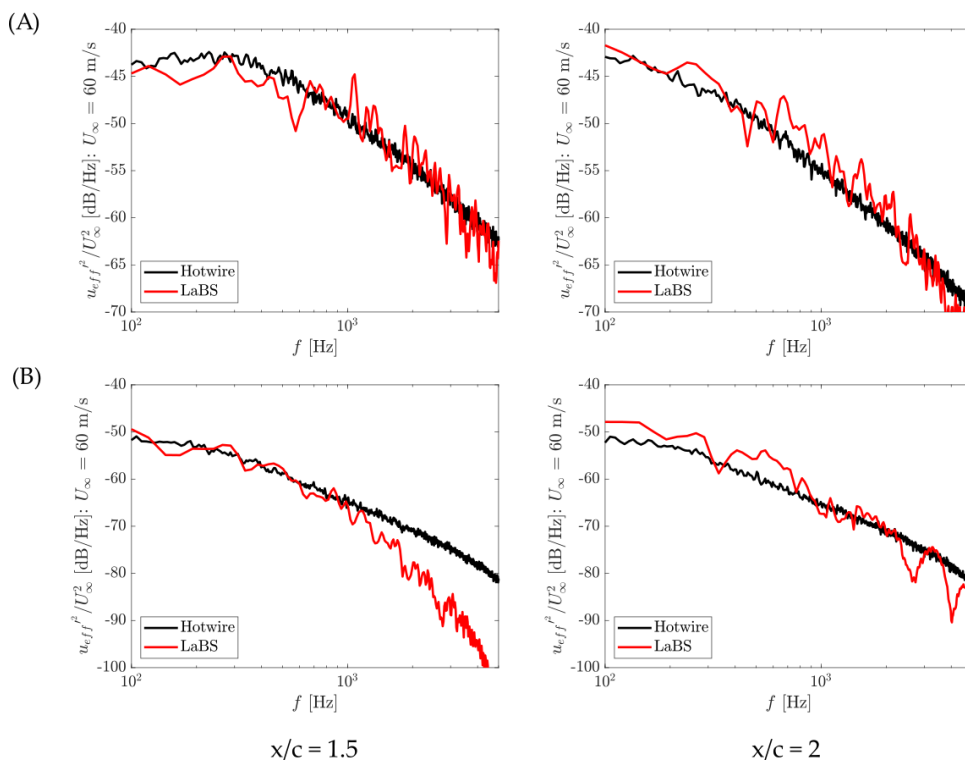


Figure 6.5: Turbulent spectra plots of the fluctuations of the effective magnitude velocity, u'_{eff} acquired at planes P1: $x/c = 1.5$ and P2: $x/c = 25$ at (A) in the location around the shear layer and the (B) along the side edge of the spoiler along the trailing edge height.

To characterise the wake convecting downstream of the spoiler, maps of the magnitude of the effective cooling velocity, U_{eff} and the component of the turbulence intensity, u'/U_{∞} were compared. The results for planes P2 and P3 are shown in Figure 6.6 and Figure 6.7 respectively.

Good agreement is observed with respect to the U_{eff} spanwise maps along the two acquisition planes selected. The wake convecting downstream of the spoiler is observed to be composed of a region of velocity deficit dominated by the bluff body recirculation vortex generated downstream of the inclined spoiler and growing free shear layers along the free edges of the spoiler. Traces of velocity deficit due to the horseshoe vortices are observed at $\frac{2y}{b} = \pm 2$.

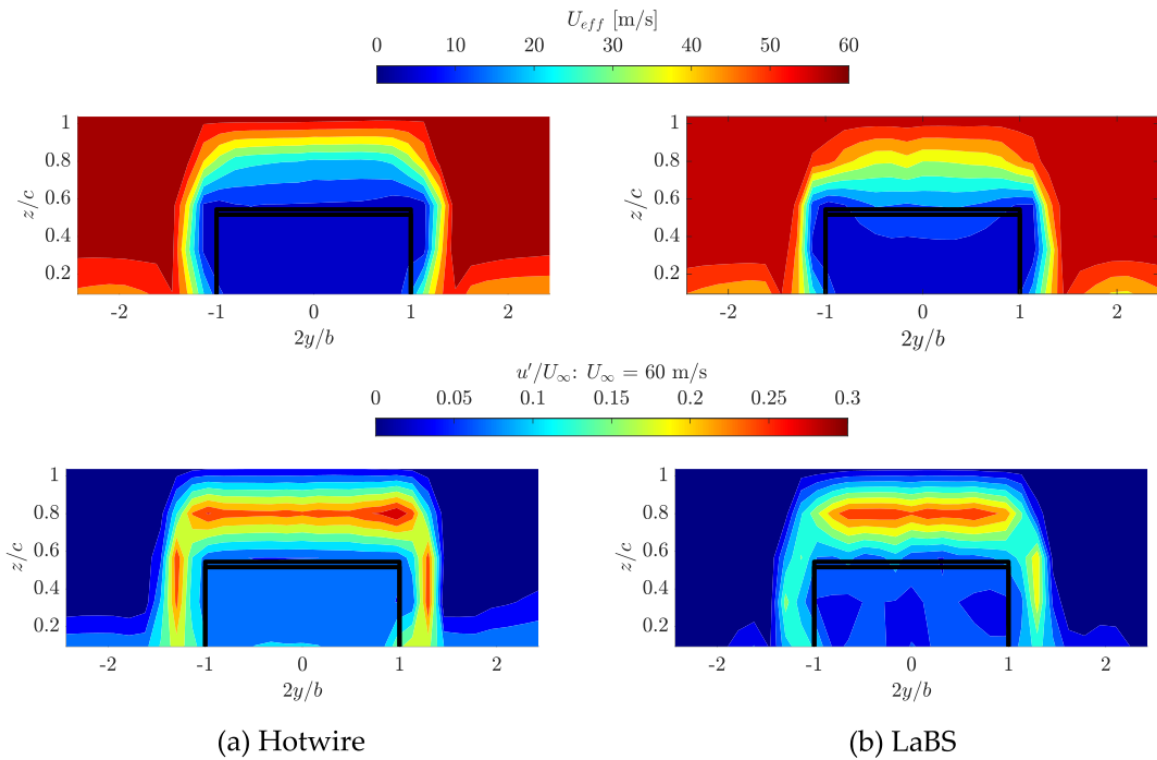


Figure 6.6: Spanwise maps of the magnitude of the effective cooling velocity, U_{eff} and the turbulence intensity due to the velocity perturbations, u'/U_∞ along plane P2 at a distance of $x/c = 1.5$ from the leading edge of the spoiler.

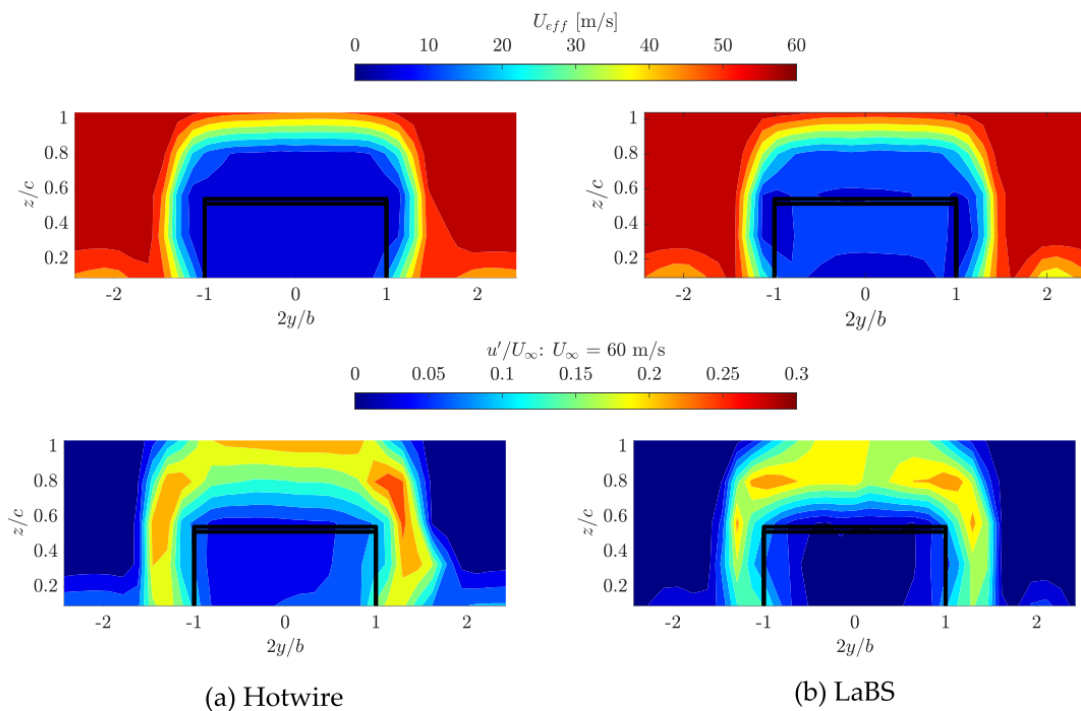


Figure 6.7: Spanwise maps of the magnitude of the effective cooling velocity, U_{eff} and the turbulence intensity due to the velocity perturbations, u'/U_∞ along plane P2 at a distance of $x/c = 2$ from the leading edge of the spoiler.

Similarly, the turbulence intensity plots show that the highest level of fluctuations are observed along the shear layers generated by the spoiler. Turbulence is observed to diffuse as the wake convects downstream from the trailing edge. Differences in the levels of turbulence intensity are observed along

regions in which rotational vortices exist, i.e. tip vortices from the trailing edge of the spoiler and the contra-rotating vortices generated along the leading edge of the spoiler. Given that the binormal perturbations, w' , behave as a second-order term when using a single hot wire probe setup, to ensure the consistency between the two methodologies, only the perturbations of the normal velocity component were considered numerically. This resulted in an under-prediction of the turbulence intensity along spanwise vertical regions.

6.3 Particle Image Velocimetry

Validation of the mean velocity flow field and the wake characteristics downstream of the trailing edge of the spoiler were done by comparing the numerical results from ProLB with those obtained from 2D PIV. The comparison was made along the streamwise symmetry plane ($y=0$ m) downstream of the spoiler. Figure 6.8 shows the comparison of the normalised mean flow velocity around the deflected spoiler at a deflection angle of 30° . Streamlines have been added to aid in visualising the location of the mean streamwise vortices.

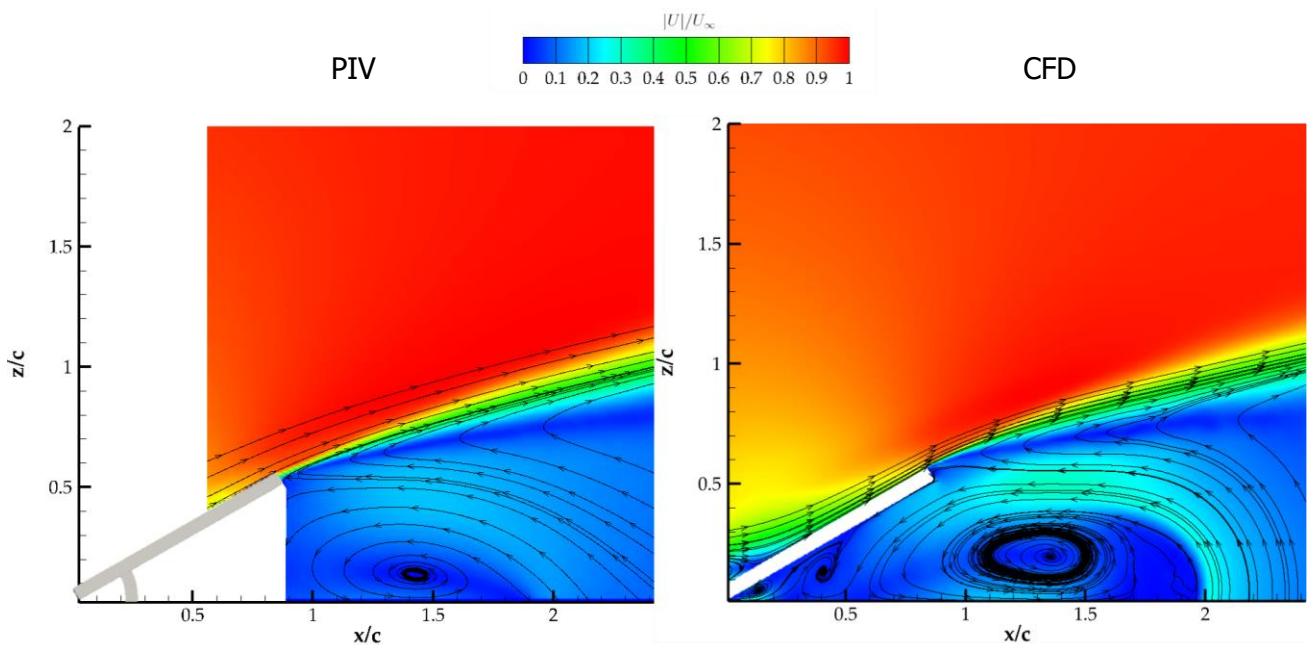


Figure 6.8: Mean flow field of the velocity magnitude $|U|$ along the streamwise symmetry plane at $y = 0$ m. Left hand image shows PIV. Right hand image shows CFD.

The mean flow field had a good agreement between experimental and numerical simulations. The wake is dominated by a bluff body recirculation region, and a growing shear layer which grows as it convects downstream. Flow from underneath of the endplate is observed to emanate upwards towards the trailing edge of the spoiler. This is due to the difference in pressure between atmospheric pressure in the quiescent flow region underneath of the endplate and the low pressure region in the wake. The emanating flow results in the formation of an extended bluff body recirculation vortex bubble downstream of the trailing edge of the spoiler.

Both methodologies identify the recirculation region at $x = 1.4c$ away from the leading edge of the spoiler. However, the numerical simulations are observed to overpredict the size of the recirculation vortex region. The flow emanating from underneath the endplate is higher when compared to that observed for the experimental results, resulting in a larger vortical structure to form. This in turn

extends the size of the bluff body recirculation region, while varying the near wall unsteady characteristics when compared to the experimental results.

Explanation of the difference in the convecting flow velocity of the two emanating flows from the trailing edge of the endplate can be summed up due to discrepancies between the conditions below the model and the nozzle between the two different methodologies. The fluid domain in the simulations does not consider the actual distance between the endplate and the floor of the anechoic chamber involving the presence of the false floor and wedges.

The increase in flow emanating from underneath of the endplate result in slightly faster wake growth to occur towards the trailing edge of the endplate. To analyse the wake growth of the wake downstream of the trailing edge of the spoiler, an analysis of the wake height growth factor k^* was analysed. The definition is shown in Equation 2.

$$k^* = \frac{\frac{\Delta z}{c}}{\frac{\Delta x}{c}}, \tag{Eq.2}$$

where z/c is the normal distance away from the wall normalised as a function of the chord of the spoiler and x/c is the streamwise distance from the leading edge of the spoiler normalised as a function of the chord. The results are shown in Figure 6.9.

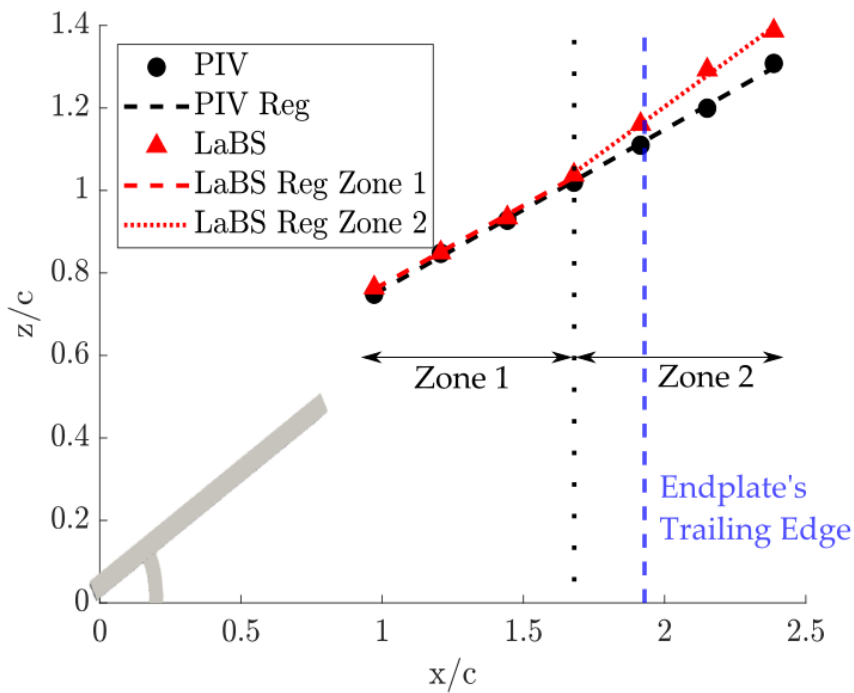


Figure 6.9: Wake height growth at different locations downstream of the spoiler.

Comparing the wake height growth with the distance downstream from the trailing edge of the spoiler, it was observed that two regions of wake height growth exist. Close to the trailing edge of the spoiler, denoted as zone 1, excellent agreement was observed between the wake height growths for the two methodologies. The difference in the wake growth height factor, Δk^* between PIV and the numerical simulations in this zone was equal to 0.004. However, as the wake convected towards the trailing edge of the endplate (denoted as zone 2), the higher momentum from the flow emanating from

underneath the endplate when compared to the PIV results, resulting in a larger wake height when compared to the experimental one. The difference in the wake growth height factor, Δk^* between PIV and the numerical simulations in zone 2, was equal to -0.112 , implying a larger wake downstream of the endplate compared to the experimental results.

Similar results were further observed for the velocity deficit profiles in the wake of a deflected spoiler at a deflection angle of 30° . The results are shown in Figure 6.10.

Three different locations were analysed. Location a is at a distance of $x/c = 1.21$ from the leading edge of the spoiler and is within zone 1, defined in Figure 6.9; (b) is at a downstream distance of $x/c = 1.68$ from the leading edge of the spoiler upstream of the endplate's trailing edge; and location (c) is at a distance of $x/c = 2.39$ from the trailing edge downstream of the endplate.

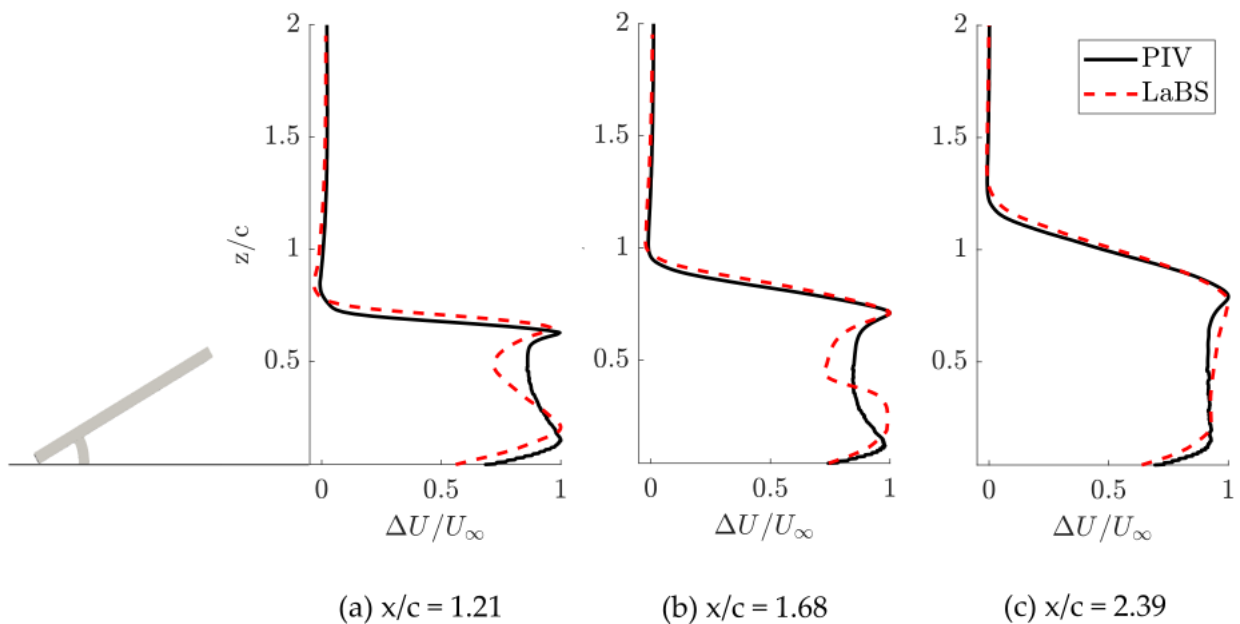


Figure 6.10: Velocity deficit profiles normalised with freestream velocity downstream of spoiler at different streamwise locations: (a) $x/c = 1.21$; (b) $x/c = 1.68$, (c) $x/c = 2.39$.

The results show that for all the three locations analysed, the shear layer growth is captured fully for the three different locations, albeit as the endplate is approached, the locations of freestream velocity is located at a higher normal distance above the endplate when compared to the experimental results.

In the upstream case shown for location (a) at $x/c = 1.21$, both methodologies capture the velocity deficit due to the recirculation region correctly however the momentum increase due to the flow emanating from underneath of the endplate is over predicted when compared to the experimental results. Along the endplate shown in location (b), it is observed that the higher vorticity induced by the flow emanating from underneath of the endplate forces the base re-circulation region to grow larger than that observed in the experimental results. Finally downstream of the endplate shown in location (c), agreement of the velocity deficit profile is observed.

6.4 Acoustic Measurements

Validation of the far-field acoustics shown in Figure 6.11 describes a comparison of the far-field noise radiated from the model, done by comparing the individual narrowband spectra calculated from both the porous and solid FW-H surfaces. These results are compared to the experimental results for the

entire model (including the endplate). To examine the directivity of the radiated pressure waves, the spectrum from three overhead locations was analysed: (a) forward arc at a polar angle $\theta = 76.25^\circ$, (b) overhead on top of the leading edge of the spoiler at a polar angle of $\theta = 89.97^\circ$ and (c) along the rearward arc downstream of the spoiler at a polar angle of $\theta = 101.5^\circ$.

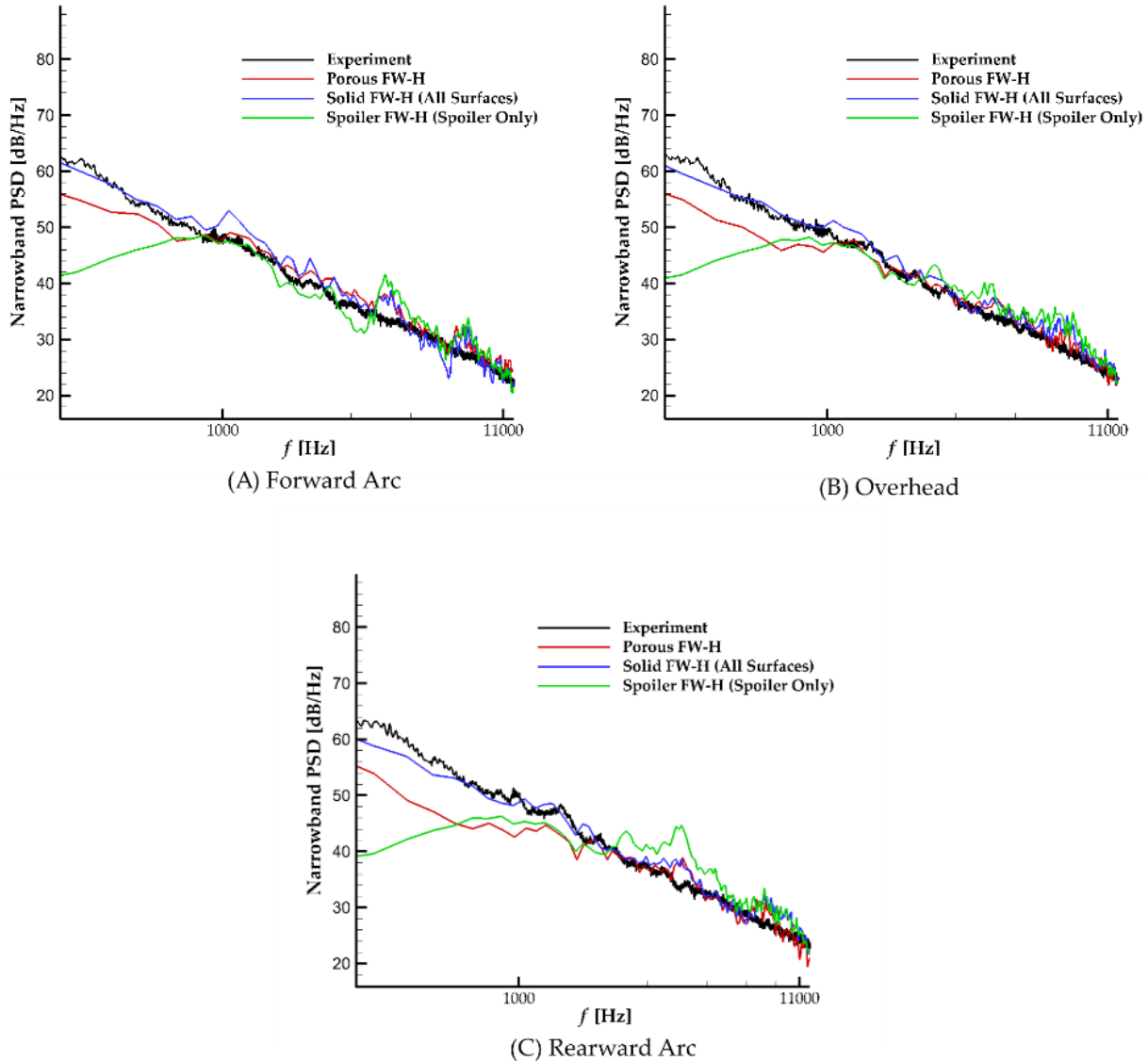


Figure 6.11: Comparison of the narrowband acoustic far-field comparison along 3 overhead locations: (a) Forward arc upstream of spoiler, (b) Directly Overhead, (c) Rearward Arc downstream of the spoiler.

In general, for the forward arc and the overhead arc, excellent agreement between the experimental results and the solid FW-H surface (for the entire model) was observed between 630 Hz and 4 kHz, with the porous surface giving better agreement than the solid FW-H surface at higher frequencies above 1 kHz. This is not the case at lower frequencies. To understand why, Figure 6.11 also shows the contribution of the deflected spoiler plate alone. The spoiler is observed to peak at a frequency of 1.25 kHz. At lower frequencies, the mounting plate dominates the farfield noise. The porous FW-H surface only contains a proportion of the flat plate. Therefore, at low frequencies, the spoiler's contribution is lower and masked by the noise radiated from the base plate, which is under-predicted by the porous FW-H calculation.

The rearward arc shows a lack of agreement between the porous FW-H surface and the solid FW-H surface for the low frequency above 2 kHz. In contrast, good agreement, within 2 dB, is observed between the experimental response and the solid FW-H surface. When analysing the porous surface, the downstream face of the porous surface is removed due to the additional hydrodynamic turbulence convecting through the surface. This alludes to the lower response at frequencies attributed to sources generated upstream of the spoiler.

The far-field noise acoustics shows that the noise generated by a deflected spoiler has a broadband nature without coherent tonal noise related to the mechanism of vortex shedding at the trailing edge of the spoiler. The flow topology shown in Figure 6.12(a) for a wall-mounted spoiler plate is observed to be defined by a turbulent wake dominated by an unsteady shear layer generated from the trailing edge of the spoiler plate, an upstream separation which results in a horseshoe vortex, and a pair of ground edge vortices which are observed to stay attached to the base mounting plate until the trailing edge of the mounting plate.

To correlate the flow features with the noise source generated by the spoiler, band-filtered on-surface pressure analysis was calculated on the solid FW-H surface at different frequencies. Figure 6.12(b) shows the unsteady fluctuations of the on-surface pressures at a narrowband frequency of 1.349 kHz. The highest on-surface fluctuation levels are observed along the ground edge vortices along the sides of the spoiler plate, the unsteady separation occurring upstream of the spoiler plate and along the hinge gap.

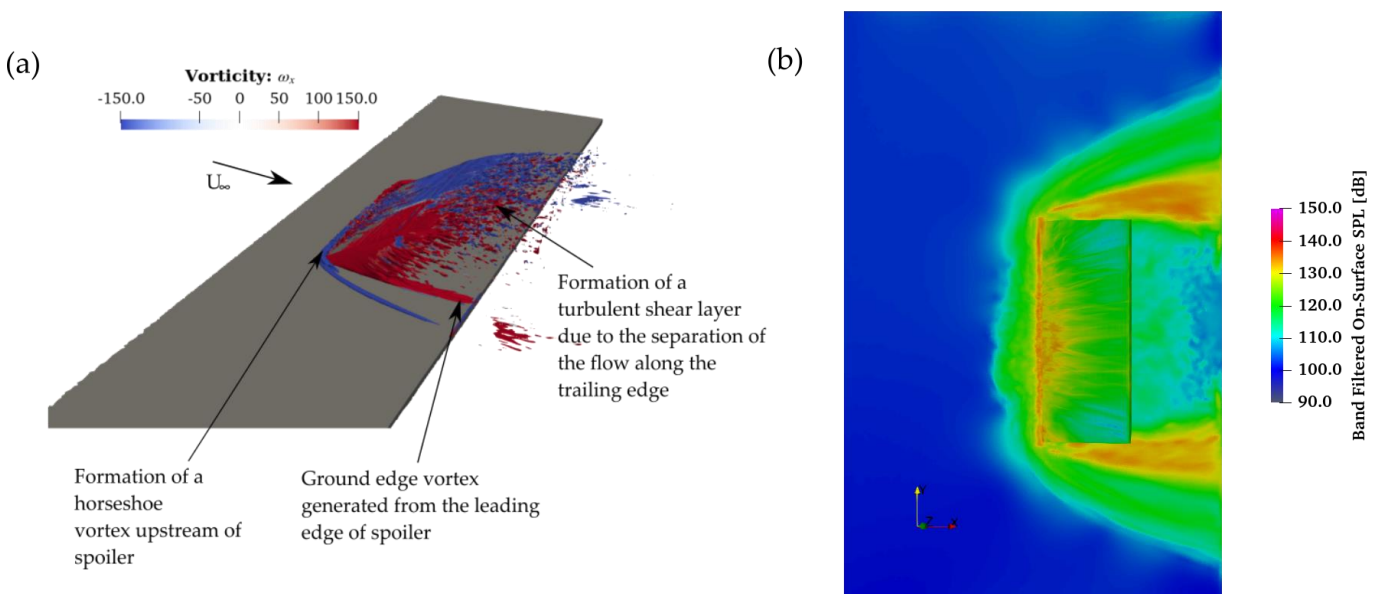


Figure 6.12: (a) Q-Criterion representation of the flow topology surrounding the inclined flat plate model at $\theta = 30^\circ$. Contour filled with the vorticity along the x-axis, ω_x . (b) Band-filtered on-surface analysis conducted for a spoiler configuration at a deflection angle of $\theta = 30^\circ$ at a narrowband frequency of 1.349 kHz.

6.5 Best Practice

While the UoS approach was to tune the cell size on the endplate in order to match the incoming boundary layer properties as closely as possible, CERFACS initiated the transition from laminar to fully turbulent flow by introducing two rows of cylinders (in staggered formation) near the wind tunnel outlet, as depicted in Figure 6.13. Each cylinder measures 2.5mm in height and 5mm in diameter.

This configuration facilitates the disruption of streaks and the formation of turbulent eddies, as illustrated in Figure 6.14. As a result, a faster time convergence is noted.

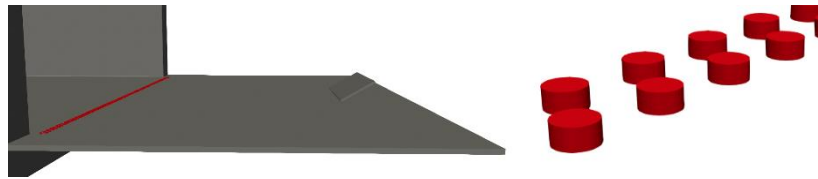


Figure 6.13: Tripping cylinders (red).

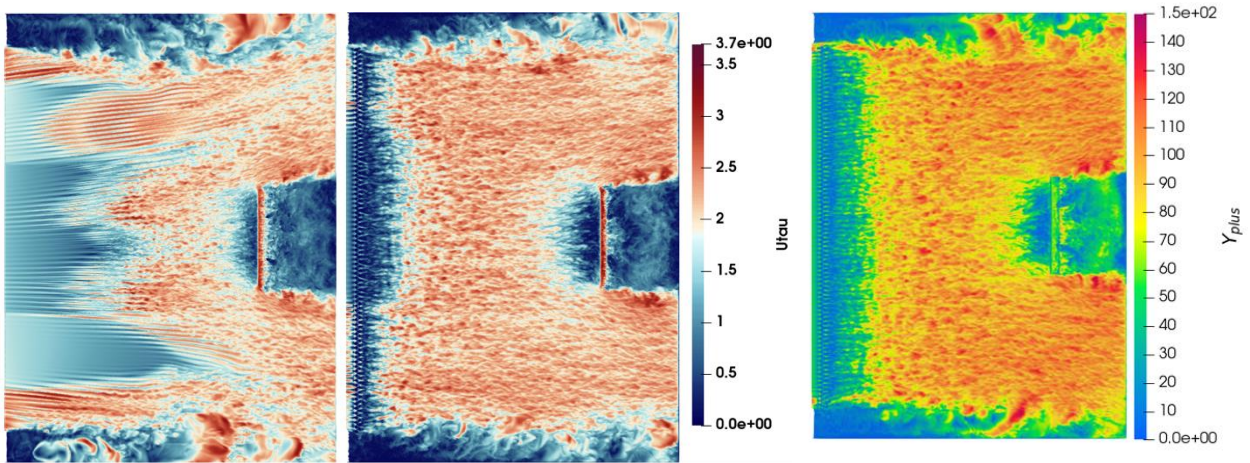


Figure 6.14: U_{tau} (from left, without and with tripping) and Y_{plus} (right) instantaneous contour on the surface of Endplate for the Extended Spoiler case.

Before delving into the main cases, a simulation was conducted using the baseline configuration to assess a sanity check from an aerodynamic standpoint. As illustrated in Figure 6.15, the simulation duration, which is longer than 4 convective times, ensures sufficient time for the forces and moments impacting the spoiler to converge effectively.

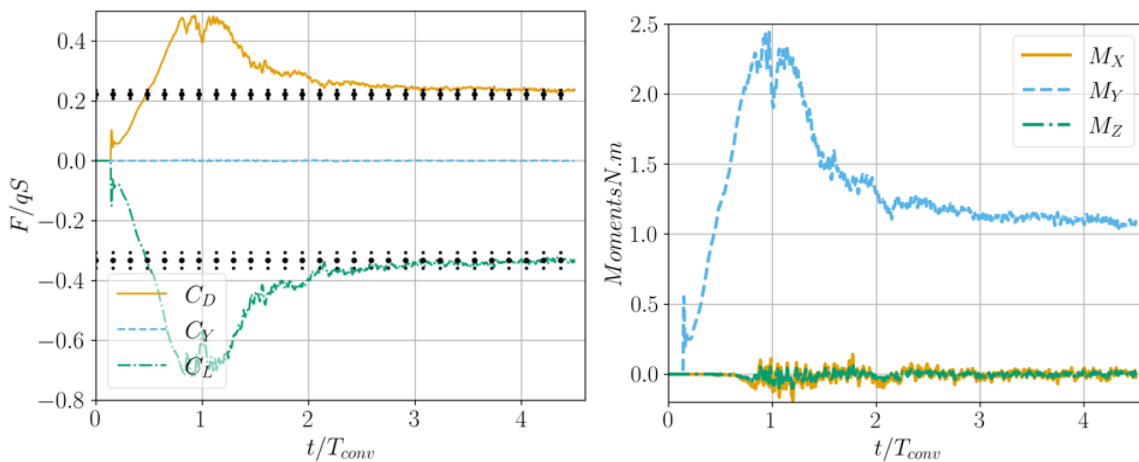


Figure 6.15: Time convergence for aerodynamic loads (left) and moments (right), baseline configuration.

On this simple geometry, the tripping does not affect the aeroacoustic data. However, it is essential to note that this may not be the case for other configurations. Indeed, the detachment point of the boundary layer on an airfoil for example is closely tied to the turbulent flow state, influencing the

wake and acoustic emissions. Ensuring the right turbulent state is crucial, and tripping could be an effective solution for this configuration.

Regarding acoustic analysis, we compare direct acoustic propagation for Ffowcs Williams Hawkings (FWH) analogy-based acoustic propagation (using porous surface data excluding the boundary layer) against experimental data.

7. Numerical Results

7.1 10 deg. Case

Simulations at a deflection angle of 10° were conducted to assess the flow topology and the noise radiated by the spoiler for a deflection in which there is a close proximity between the spoiler plate and the mounting surface. Figure 7.1 shows a comparison of the far-field acoustics conducted by comparing the narrowband spectra for the wall-mounted spoiler for three polar locations along the overhead flyover arc at a polar angle of: (a) forward arc at a polar angle $\theta = 76.25^\circ$, (b) overhead on top of the leading edge of the spoiler at a polar angle of $\theta = 89.97^\circ$ and (c) along the rearward arc downstream of the spoiler at a polar angle of $\theta = 101.5^\circ$. A comparison between the experimental far-field spectra and the numerical spectra calculated from the porous and solid FW-H surfaces was provided.

For each flyover polar angle presented, agreement is observed for both the solid FW-H surface and the porous FW-H surface between 506 Hz up to a frequency of 1 kHz. The porous FW-H surface showed better agreement up to 1 dB with respect to the experimental results. For lower frequencies, in which the main noise contributor is the noise generated by the endplate, a better approximation is observed with the solid FW-H surface, in which the noise from the whole endplate was considered.

At frequencies above 1 kHz, disagreement in the noise level is observed between the experimental and the numerical results, albeit the same trends are observed. For the experimental results, when the spoiler is deflected at shallow angles, a broadband hump is observed in the frequency range between 1.46 kHz and 1.78 kHz, resulting in a +5 dB increase to the power spectral amplitude for the noise being radiated at that frequency. Similarly, for both the solid and porous FW-H surfaces, an increase in the power spectral density amplitude is observed in the form of a broadband hump at a slightly lower frequency of 1.34 kHz but at a much higher amplitude equal to +21.5 dB. Secondary harmonics are observed at $f_2 = 2.69$ kHz and $f_3 = 4.45$ kHz, respectively. In comparison to the narrowband noise spectra calculated from the spoiler's solid surface, at low frequencies below 1 kHz, the main source of noise radiation is the endplate, with the noise from the spoiler becoming significant above 1 kHz.

To understand the source of the broadband hump observed at 1.34 kHz, an on-band filtered analysis was conducted on the solid FW-H surface at the given frequency shown in Figure 7.2. The results obtained show that a localised region of high fluctuation amplitude is observed between the downstream face of the spoiler and the endplate, implying that the broadband hump is generated due to the flow emanating through the hinge and the resultant reflections of the standing wave between the two adjacent surfaces.

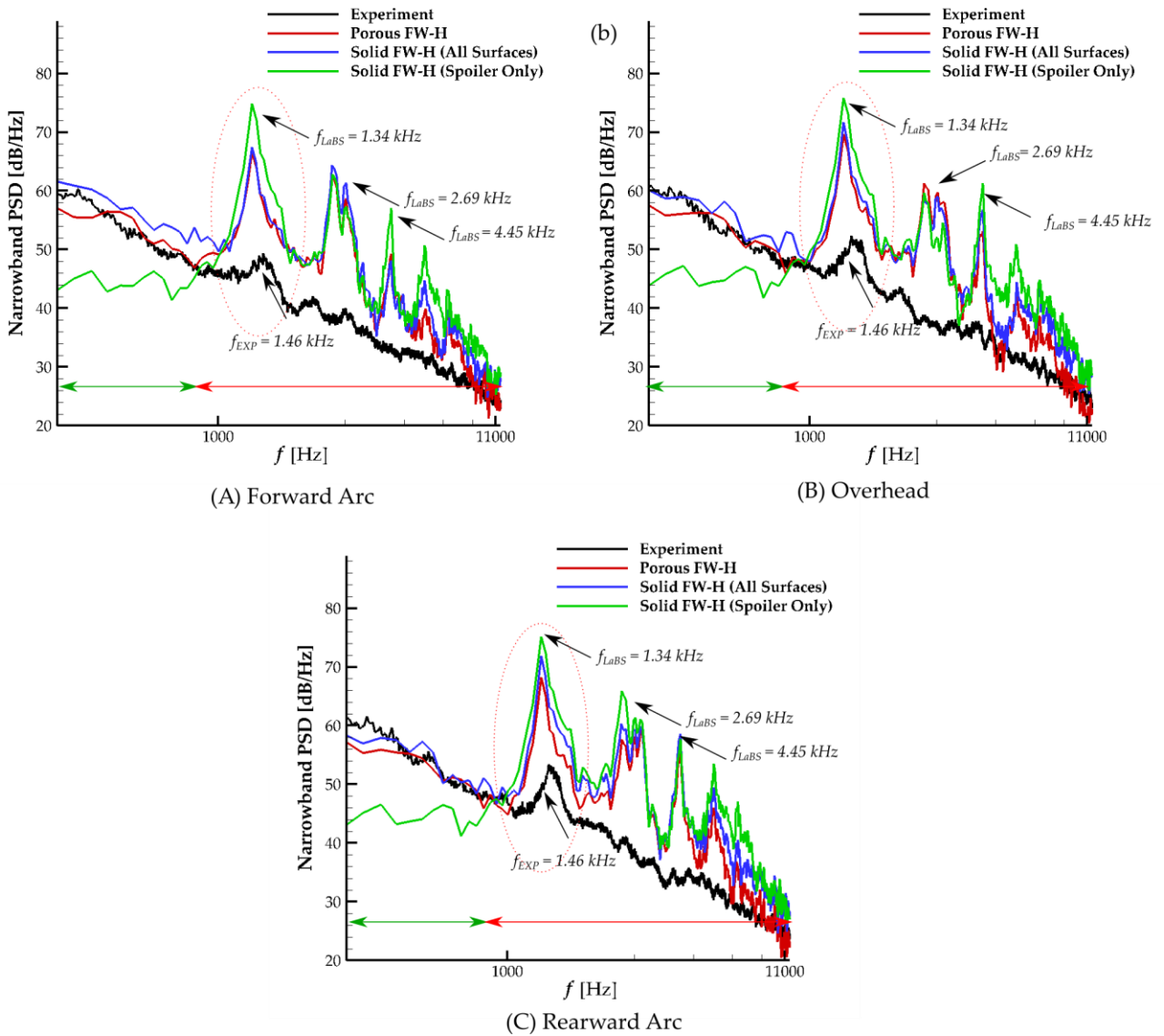


Figure 7.1: Comparison of the narrowband acoustic far-field comparison along 3 overhead locations: (a) Forward arc upstream of the spoiler, (b) Directly Overhead, (c) Rearward Arc downstream of the spoiler.

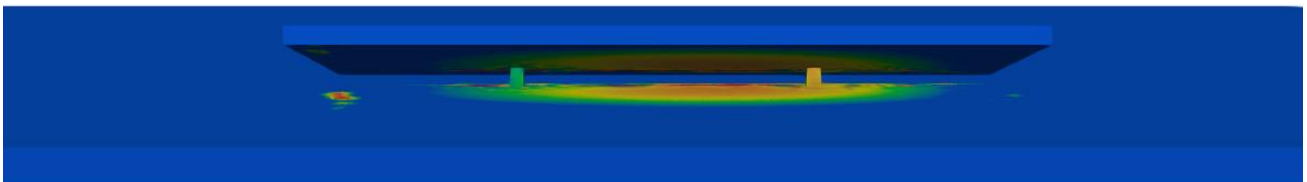
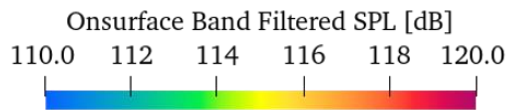


Figure 7.2: On-surface frequency band filtered SPL at a frequency, $f = 1.34$ kHz along the hinge gap calculated on the solid FW-H surface.

Figure 7.3(a), shows the mean flow field of the velocity magnitude along the streamwise symmetry plane of the wall-mounted spoiler plate. Within the cavity formed between the downstream surface

of the spoiler and the endplate, the main flow direction is observed to be dictated by the reversed flow along the base region. As such, this creates the formation of a tapered open-air column, potentially resulting in a standing waveform between the two surfaces.

Due to the high-velocity flow emanating through the hinge gap, two vortices are observed to form. An initial vortex forms along the hinge exit as a result of the shear force generated from the emanating flow from the hinge gap which is at a much higher velocity than the cavity flow. Additionally, a secondary vortex of opposite vorticity is observed to form downstream of this initial hinge vortex. These flow features due to flow through the hinge gap result in the effective increase in the hinge noise when compared to experimental results.

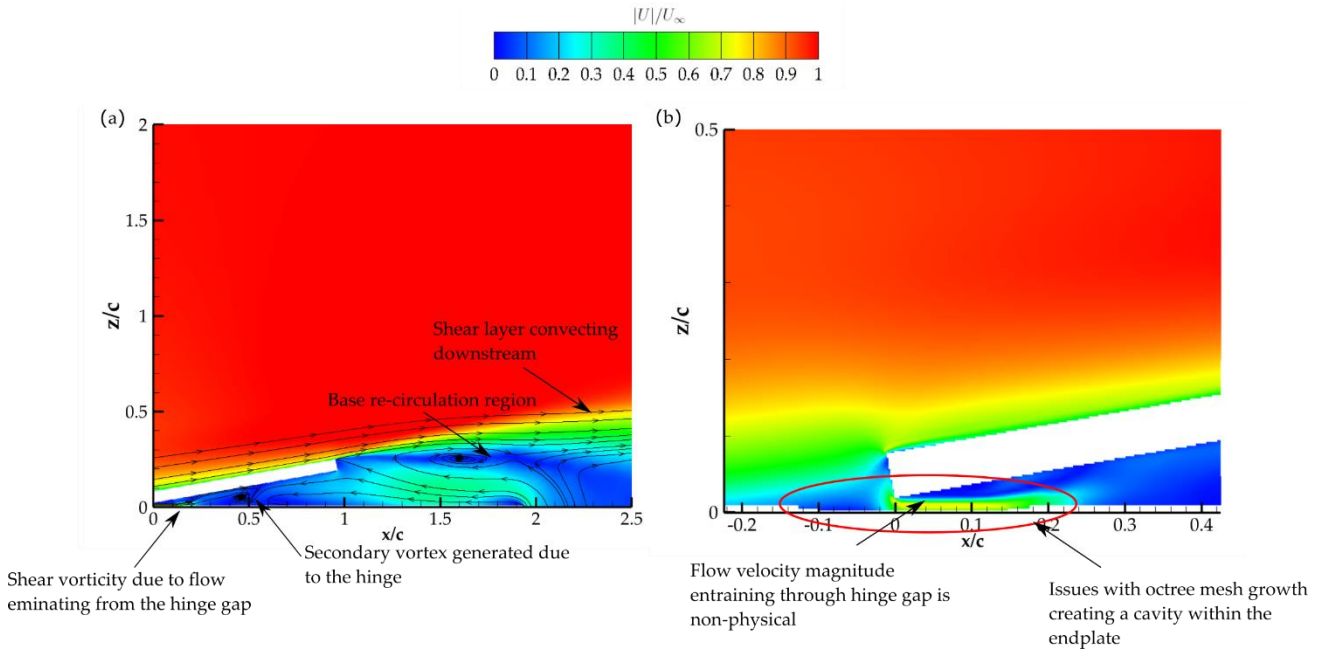


Figure 7.3: (a) Mean flow field of the velocity magnitude $|U|$ along the streamwise symmetry plane at $y = 0$ m. (b) Flow emanating through the hinge gap between the leading edge of the spoiler and the endplate.

Figure 7.3(b) highlights the hinge gap region for a spoiler deflected at 10° . The flow emanating through the hinge is observed to reach a magnitude of $0.7U_\infty$, which is deemed to be non-physical given that the hinge gap lies within the boundary layer of the incoming flow velocity. Better understanding of the flow emanating through the hinge can be observed by assessing the mesh across the hinge gap. ProLB uses a Cartesian/octree mesh generator to generate cells according to the refinement region specified. This is done automatically by the solver. A refinement of $\Delta x = 0.25$ mm was selected across the hinge gap to ensure enough cells were in this region to resolve the flow through the hinge gap. This said, due to the close proximity of the leading edge of the spoiler and the endplate, to allow for enough cells to form within the gap, a stepped cavity is formed within the endplate surface through which flow emanating. This is a result of the automated meshing as part of ProLB. This results in higher flow velocities through the gap when compared to the experimental results and hence higher on-surface pressure fluctuations along the hinge gap and the surrounding surfaces. This results in an over prediction in the acoustics when to the experimental results for the effected frequencies.

To assess the impact of the flow emanating through the hinge gap between the leading edge of the spoiler and the endplate, a comparison of the far-field spectra with a blocked hinge comparison was

done, shown in Figure 7.4. A uniform rectangular strip was modelled allowing for uniform cell growth along the surfaces without changing the location of the leading edge of the spoiler. Figure 7.4 shows the mean flow field of the velocity magnitude along the stream wise symmetry plane comparison for the two configurations.

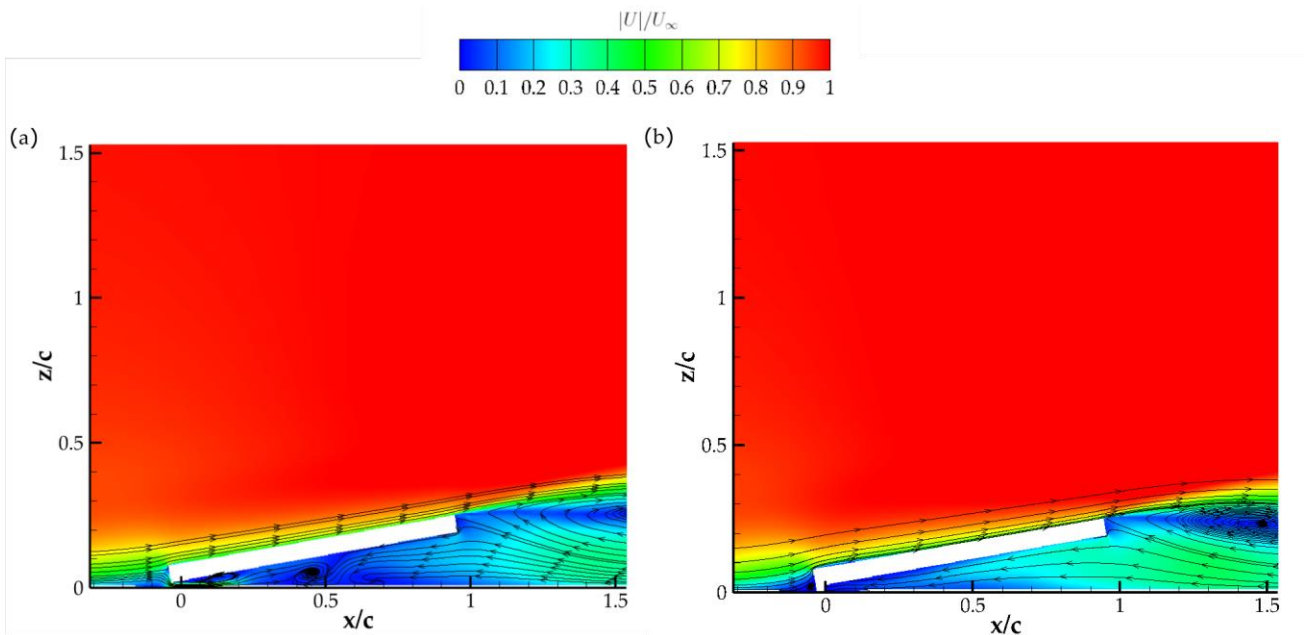


Figure 7.4: Comparison of the velocity magnitude and the streamlines of the flow surrounding the deflected wall-mounted spoiler for the configuration when the hinge gap is (a) open, (b) blocked.

By blocking the gap between the leading edge of the spoiler and the endplate, no flow is allowed to emanate through the gap. As a result, the two impinging vortices which were created due to the shear force generated by the emanating flow do not exist. The reverse flow along the base region, which convects towards the trailing edge of the spoiler, is observed to flow through the formed cavity at a higher velocity magnitude due to the lack of adverse pressure formed from the flow the higher flow in the opposite direction through the hinge. This results in forming a closed tapered air column with a standing wave reflecting along the two adjacent surfaces.

A comparison of the far-field results obtained from the porous FW-H surfaces was done with respect to the experimental results for the same configuration having the hinge gap blocked using tape. The results obtained are shown in Figure 7.5, for three overhead flyover arc polar angles of : (a) Forward arc at a polar angle $\theta = 76.25^\circ$, (b) overhead on top of the leading edge of the spoiler at a polar angle of $\theta = 89.97^\circ$ and (c) along the rearward arc downstream of the spoiler at a polar angle of $\theta = 101.5^\circ$.

In general, for the three locations analysed, improved agreement between the porous FW-H surface and the experimental far-field results was obtained for all three polar angles. When the hinge gap is blocked, the disagreement between the two spectra along the range of frequencies dictated by the noise due to the flow emanating through the hinge gap falls to 3 dB. Additionally, a broadband increase is observed in the region between 700 Hz and 1.25 kHz. The flow within the cavity resembles a closed air column with a resonant standing wave reflecting along the two surfaces. From theory of the fundamental frequency for an air column open at one end can be calculated as shown in equation

3, where f_1 is the fundamental of the standing wave, L is the length of the column and a is the speed of sound in air.

$$f_1 = \frac{a}{4L} \tag{Eq.3}$$

Assuming that the deflection angle is small enough such that the $\sin(\theta)$ tends to 0, the projected geometry of the deflected spoiler can be assumed to be similar to that of the flow passing through the one open ended cylinder. Considering that the length of the air column is equal to the projected area of the spoiler on the endplate equal to 0.104, the first fundamental frequency $f_1 = 817$ Hz lies within the broadband hump region which exhibits for a closed hinge study. Discrepancies to the fundamental frequency lies from the fact that for a deflected spoiler, a spanwise length exists which leads to the formation of other spanwise nodes which are not considered. Other discrepancies are dictated by the fact that the effective blockage was not done the same way experimentally and numerically and that the flow emanating inwards along the sides of the spoiler is not considered. Agreement with the experiment is observed to get worse in downstream directions, as for larger polar angles, the mid to high frequencies are observed to be underpredicted.

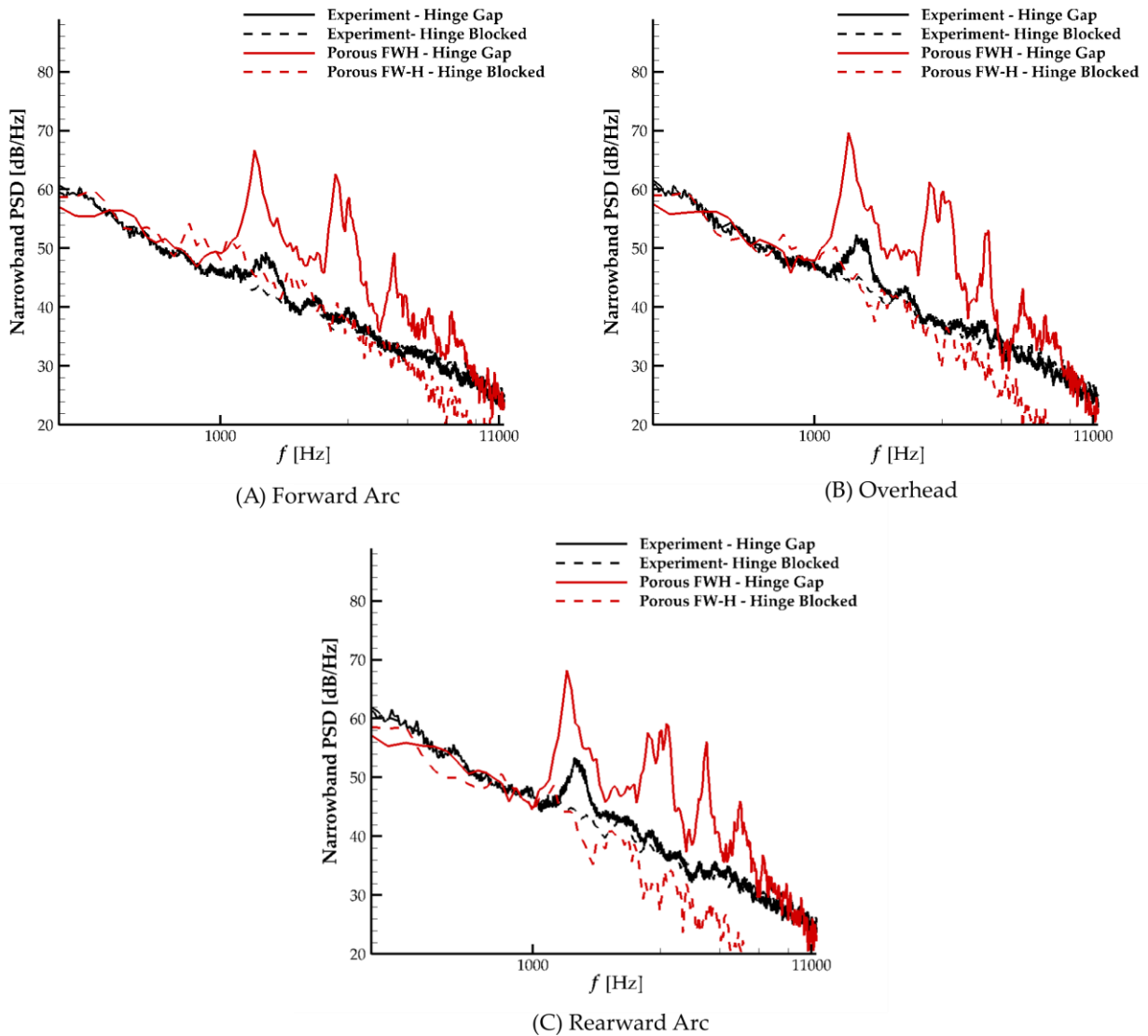


Figure 7.5: Comparison of the acoustic far-field narrowband spectra comparing the far-field spectra analysed by experimental and numerical methodologies for the hinge gap open and the hinge gap blocked.

Figure 7.6 shows the ΔSPL difference for the one-third octave spectrum obtained for the two hinge conditions analysed. This was done by assessing the ΔSPL_{hinge} , whose equation is provided in Equation 4, comparing the impact of blocking the hinge gap experimentally (shown in Figure 7.6 (a)) and numerically (shown in Figure 7.6(b)).

$$\Delta SPL_{hinge} = SPL_{blocked} - SPL_{open} \quad \text{Eq.4}$$

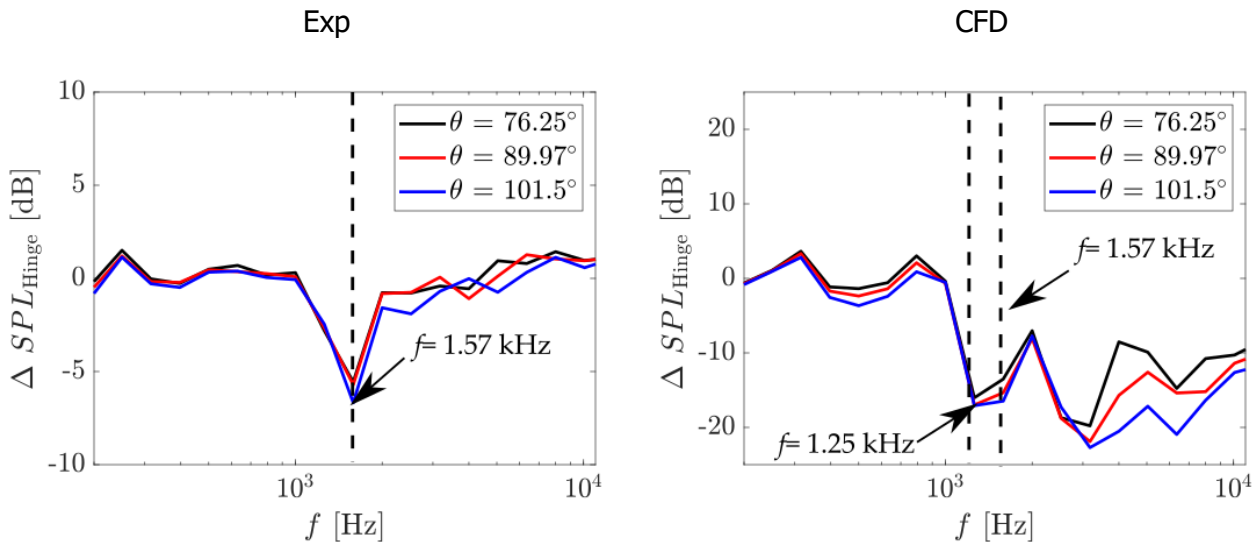


Figure 7.6: ΔSPL [dB] for the one-third octave spectrum between the effective noise reduction by physically blocking the hinge gap. Spoiler deflection angle 30° .

The effect of blocking the hinge gap resulted in a reduction in the overall noise at a one-third octave along the frequency between 1 kHz and 2 kHz. A reduction of -5 dB was observed for the experimental results, whereas the low frequency and high frequencies saw smaller changes on the magnitude of ± 1 dB. Similar trends were observed for the results obtained by the numerical simulations, this said, the magnitude of the differences were larger. Additionally, a reduction in the secondary peaks were also observed whose magnitude of the ΔSPL reduction with the blockage varied with flyover polar angle.

The flow topology of the flow generated by a wall-mounted spoiler deflected at an angle of 10° , is shown in Figure 7.7. Compare to the validation configuration at a deflection angle of 30° , the upstream separation and subsequent formation of horseshoe vortices are much weaker. Flow is observed to stay attached to the upstream face of the spoiler and is observed to separate along the trailing edge resulting in the formation of a turbulent shear layer. An analysis of the turbulence perturbations along the shear layer was conducted as shown in Figure 7.8. Similar, to the baseline case no coherent vortex shedding was observed. Additionally, the peak observed at 1.4 kHz relates to unsteady fluctuations generated from the flow emanating through the hinge gap of the spoiler. Lower amplitude of fluctuations are found when compared to the validation case, suggesting that the turbulence perturbations in the shear layer is a function of the deflection angle of the spoiler, and hence the projected area incident with the freestream velocity.

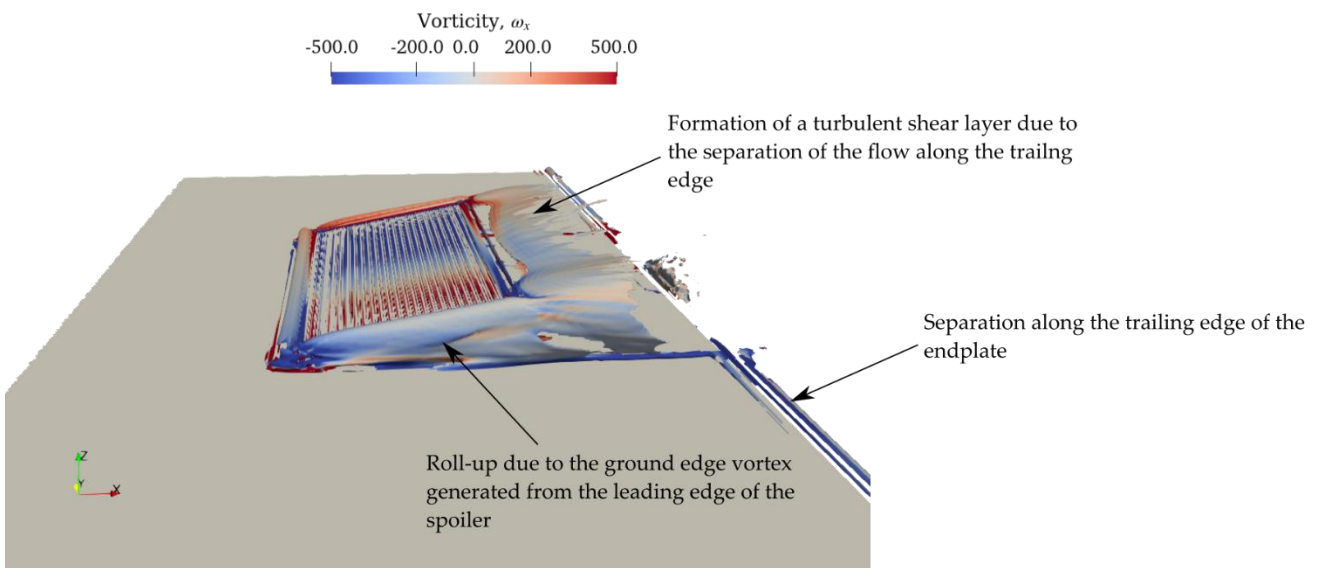


Figure 7.7: Q-Criterion representation of the flow topology surrounding the inclined flat plate model at $\theta = 10^\circ$. Contour filled with the vorticity along the x-axis, ω_x .

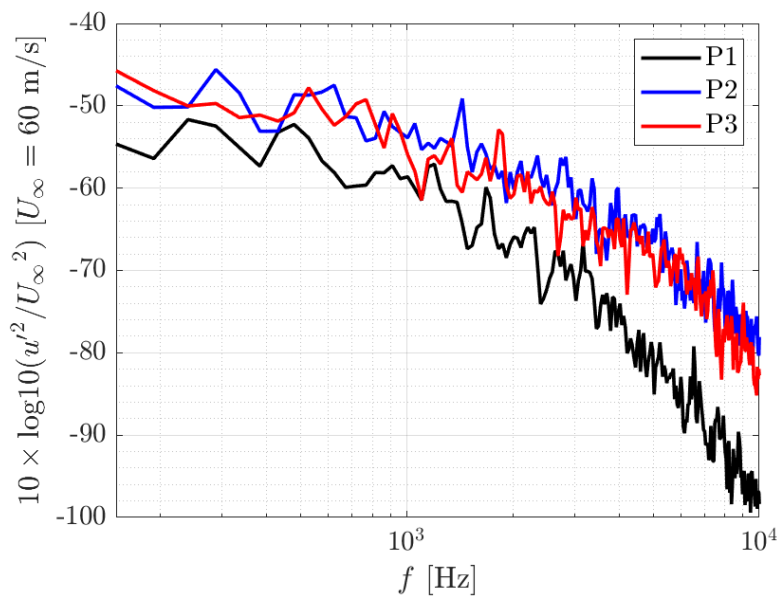


Figure 7.8: Turbulent Spectra plots of the fluctuations of the effective magnitude velocity, u'_{eff} acquired at planes P1: $x/c = 1.5$ and P2: $x/c = 2$ along the shear layer

7.2 90 deg. Case

Simulations at a deflection angle of 90° were conducted to assess the flow topology and the noise radiated by the spoiler for a deflection angle in which the spoiler is normal to the flow.

A comparison of the narrowband far-field acoustic data was done between the experimental results and the numerical solid FW-H surfaces and is shown in Figure 7.9. Due to the size of the wake, the far-field results obtained by the porous surface were not included, given the fact that turbulence in the wake was convecting through the porous surfaces, leading to an overall increase in the pressure perturbations in the FW-H equation. Therefore, this data is not presented.

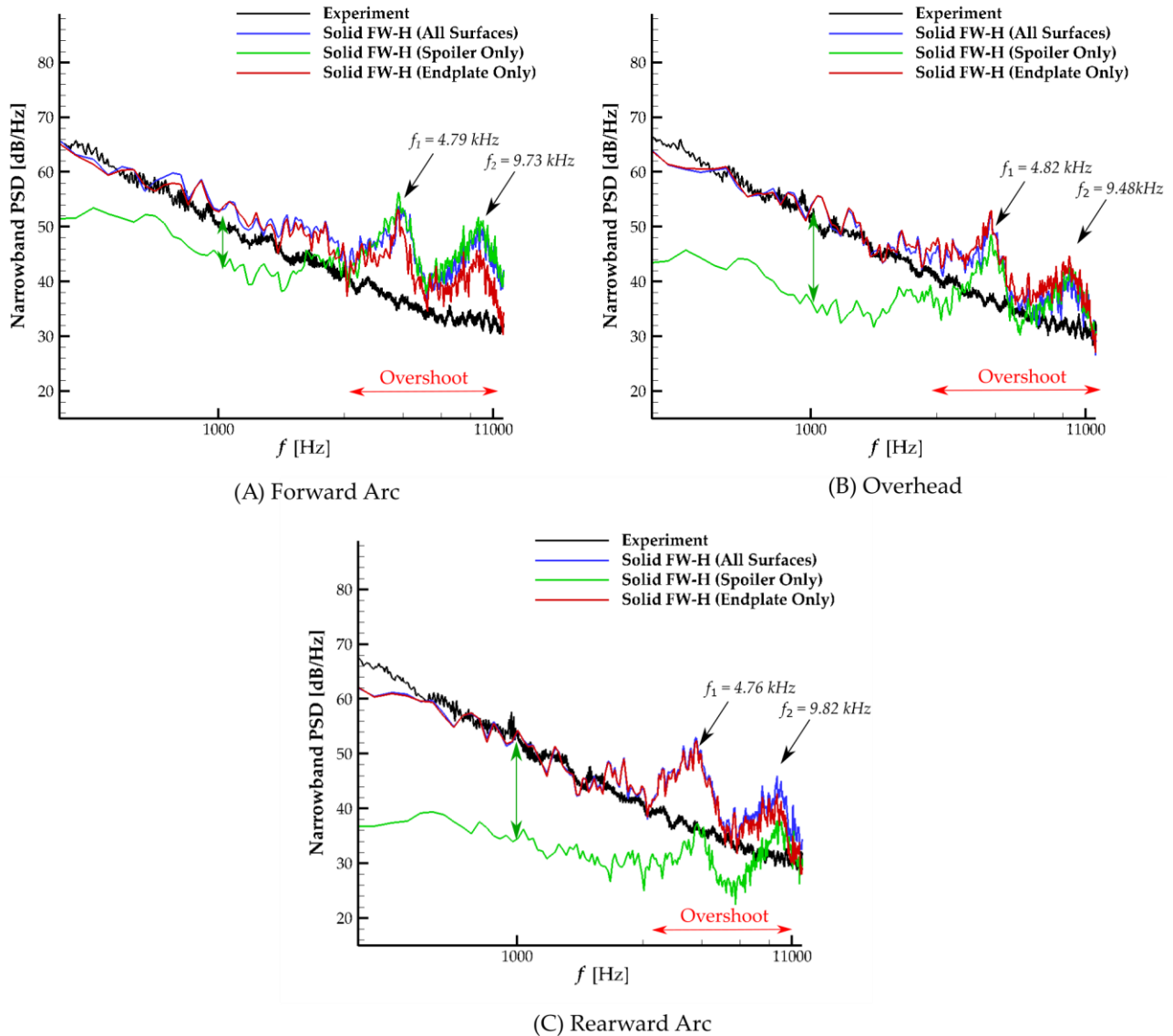


Figure 7.9: Comparison of the narrowband acoustic far-field for the wall-mounted spoiler deflected at a deflection angle of 90° along 3 overhead locations: (a) Forward arc upstream of spoiler, (b) Directly Overhead, (c) Rearward Arc downstream of the spoiler.

Agreement between the two sets of methodologies is observed up until 3 kHz, with the best agreement observed within 1 dB for the rearward arc downstream of the spoiler between the narrowband frequencies of 464 Hz and 3 kHz. To assess the contribution of the noise generated by the different components of the wall-mounted spoiler, Figure 7.10 also presents the far-field narrowband spectra from the endplate surface and the spoiler surface. Beyond 3 kHz, the numerical spectrum overestimates the far-field noise radiated by the solid surface when compared to the experimental results. In addition, two broadband humps are observed at 4 kHz and 9 kHz. A comparison of the on-surface band-filtered fluctuations for each respective frequency, shown in Figure 7.10, showed that for these two particular frequencies, a zone of high fluctuations is observed downstream of the hinge gap of the spoiler along a line that spans the width of the spoiler plate. The

streamwise location of such a line corresponds to the edge of the stepped cavity, which forms along the hinge gap of the spoiler (shown in Figure 7.11).

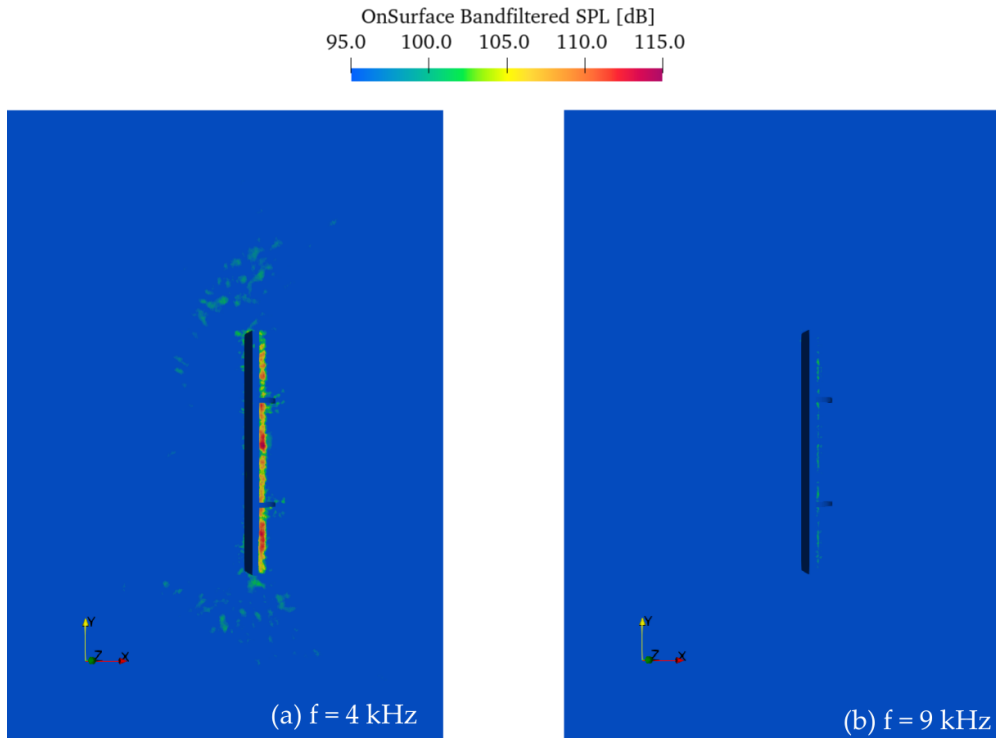


Figure 7.10: Frequency on-surface band-filtered analysis conducted on the Solid FW-H surface for the two frequencies (a) 4 kHz and (b) 9 kHz showing broadband humps in the narrowband spectra

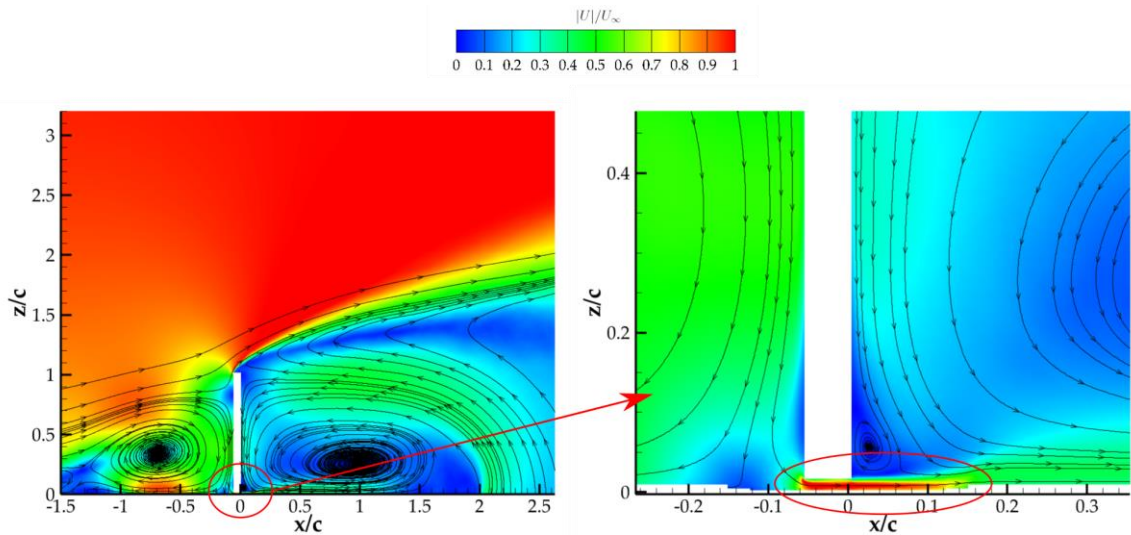


Figure 7.11: Mean flow field of the velocity magnitude $|U|$ along the streamwise symmetry plane at $y = 0$ m. Issues with the mesh generation along the hinge in which to allow for enough cells along the surface a stepped cavity forms along the hinge gap resulting in a non-physical flow velocity emanating from the hinge.

The formation of this stepped cavity induces higher flow rates through the hinge gap, which in turn results in an emanating flow downstream of the hinge equal to approximately the freestream velocity. This is non-physical and an artefact of the mesh generation process. The interaction of this hinge flow and the stepped mesh topology results in a noise source to form at high frequencies. Finer local

mesh sizes along the gap and downstream of the spoiler could be used to further refine these regions and reduce this effect.

Unlike the previous configurations discussed in which the contribution of the spoiler is observed to peak at 1.25 kHz, for the case when the spoiler is deflected normal to the incoming freestream velocity, the noise contribution from the spoiler is observed to be significantly lower than that from the endplate. Figure 7.12 shows the directivity plots of the contribution of the A-weighted overall sound pressure levels (A-OSPL) for the individual solid surfaces from the endplate and the spoiler along the overhead flyover arc. The A-weighted overall sound pressure levels for the spoiler surface are observed to reduce with an increase in the polar angle, and is observed to dip suddenly after a polar angle of $\theta = 90^\circ$, which corresponds to the receiver which is directly on top of the trailing edge. This implies, that the noise source of the spoiler occurs along the upstream face of the spoiler, and hence for larger polar angles, the noise radiation to farfield is physically masked by the deflected plate.

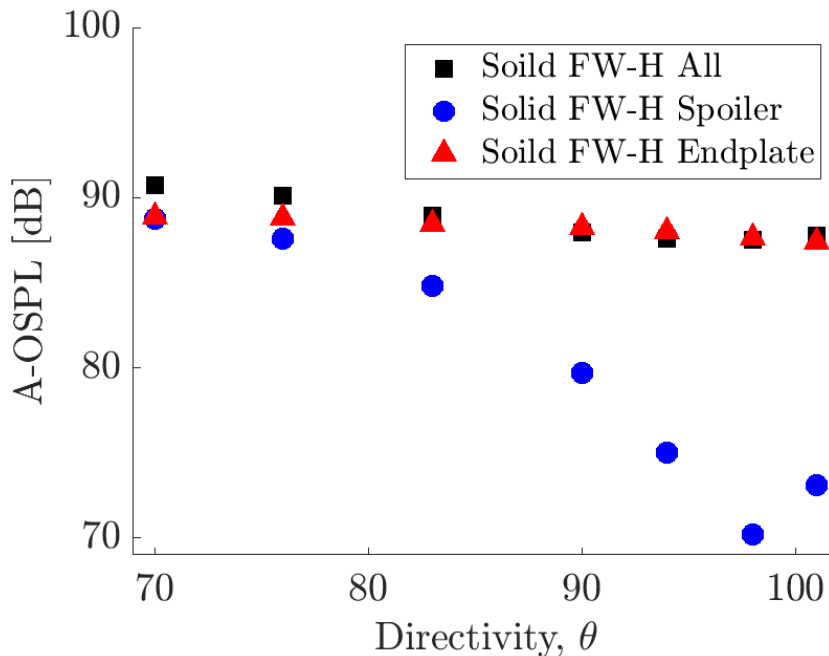


Figure 7.12: A-weighted overall sound pressure levels comparing the noise contribution from the spoiler and the endplate.

Similar results are obtained when analysing the unsteady on-surface bandwidth filtered frequency for the narrowband frequencies below 3 kHz, shown in Figure 7.13. Comparison to the flow topology presented from the Q-criterion plot in Figure 7.14 shows that for larger deflection angles, the predominant noise source is the separation occurring upstream of the spoiler and the large turbulent wake generated. This leads to regions of higher on-surface fluctuations along the endplate and the upstream face of the spoiler when compared to the downstream surface of the spoiler. Additionally, although the two contra-rotating ground edge vortices are still significant noise sources, as shown in Figure 7.13(a), the highest intensity is located along the endplate in the regions where the horse shoe vortex deflects around the free sides of the spoiler.

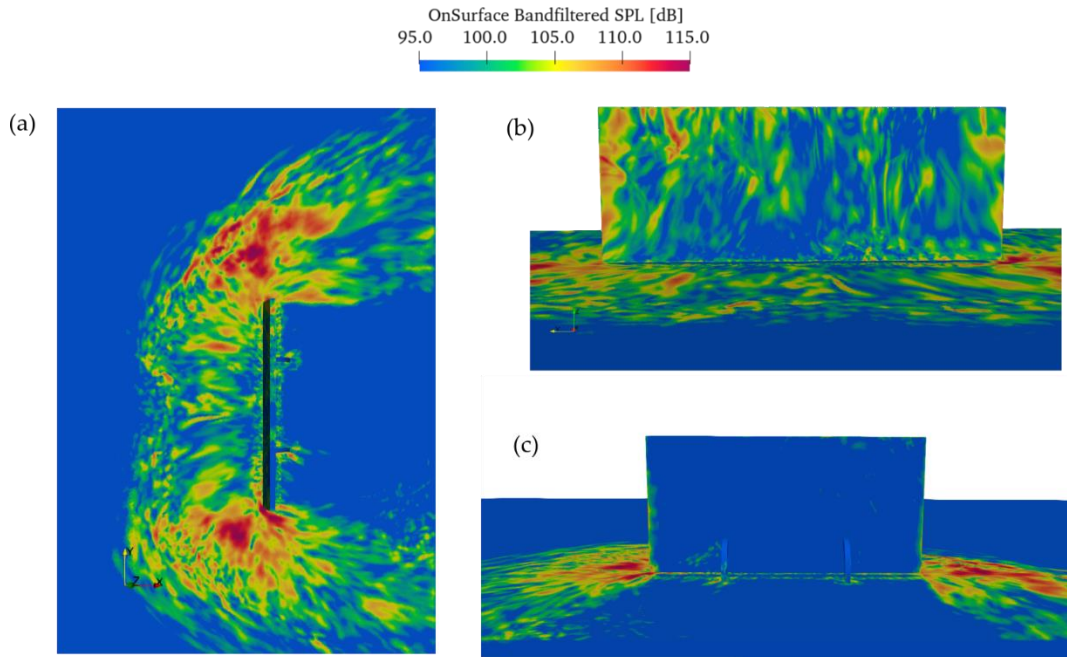


Figure 7.13: Frequency on-surface band filtered fluctuations at $f = 1.35$ kHz for a spoiler deflected at a deflection angle of 90° showing the different views along the solid FW-H surface: (a) Endplate; (b) Upstream spoiler face; (c) Downstream spoiler.

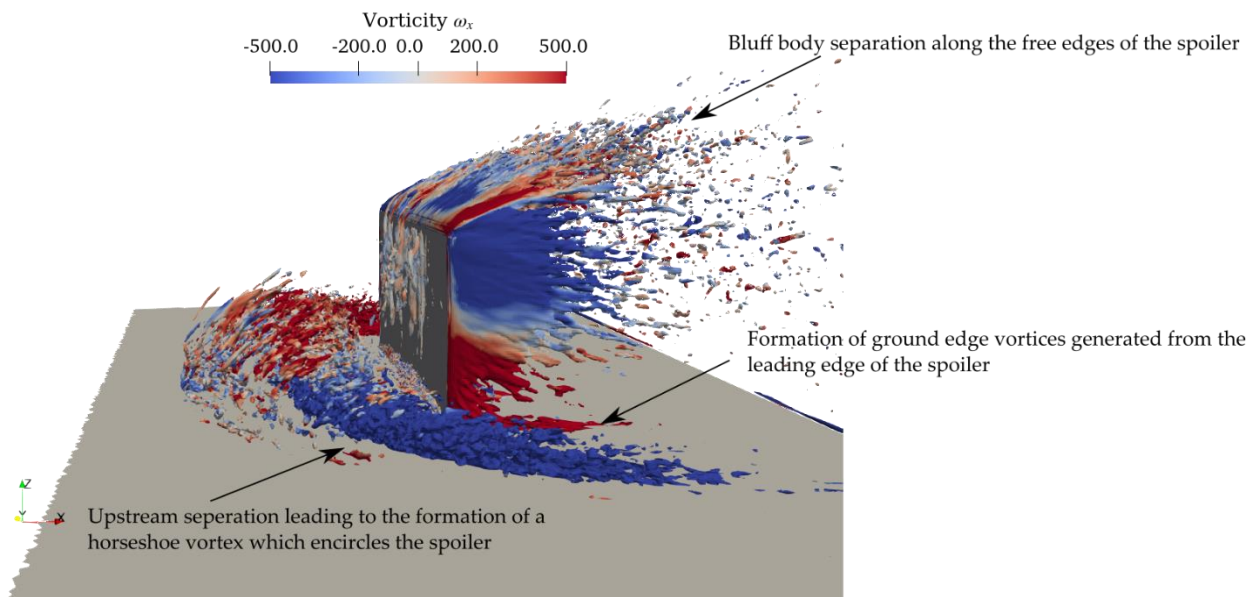


Figure 7.14: Q-Criterion representation of the flow topology around the inclined flat plate model at $\theta = 90^\circ$. Contour filled with the vorticity along the x-axis, ω_x .

7.3 Extended Chord

As shown in Figure 7.15 below, for the extended chord case, the results from two different acoustic measurements techniques demonstrates good agreement with the experimental data (XP) in the frequency range between 4 and 10 Strouhal numbers. At lower Strouhal numbers, the underestimation of experimental data from direct microphones acquisition gradually diminishes with a larger directivity angle. Conversely, data from FWH surfaces is more direction-independent. For

Strouhal numbers greater than 10, the cutoff frequency of the direct acquisition spectra is nearly unaffected by the directivity angle, and a similar behaviour is observed for the FWH surfaces spectra.

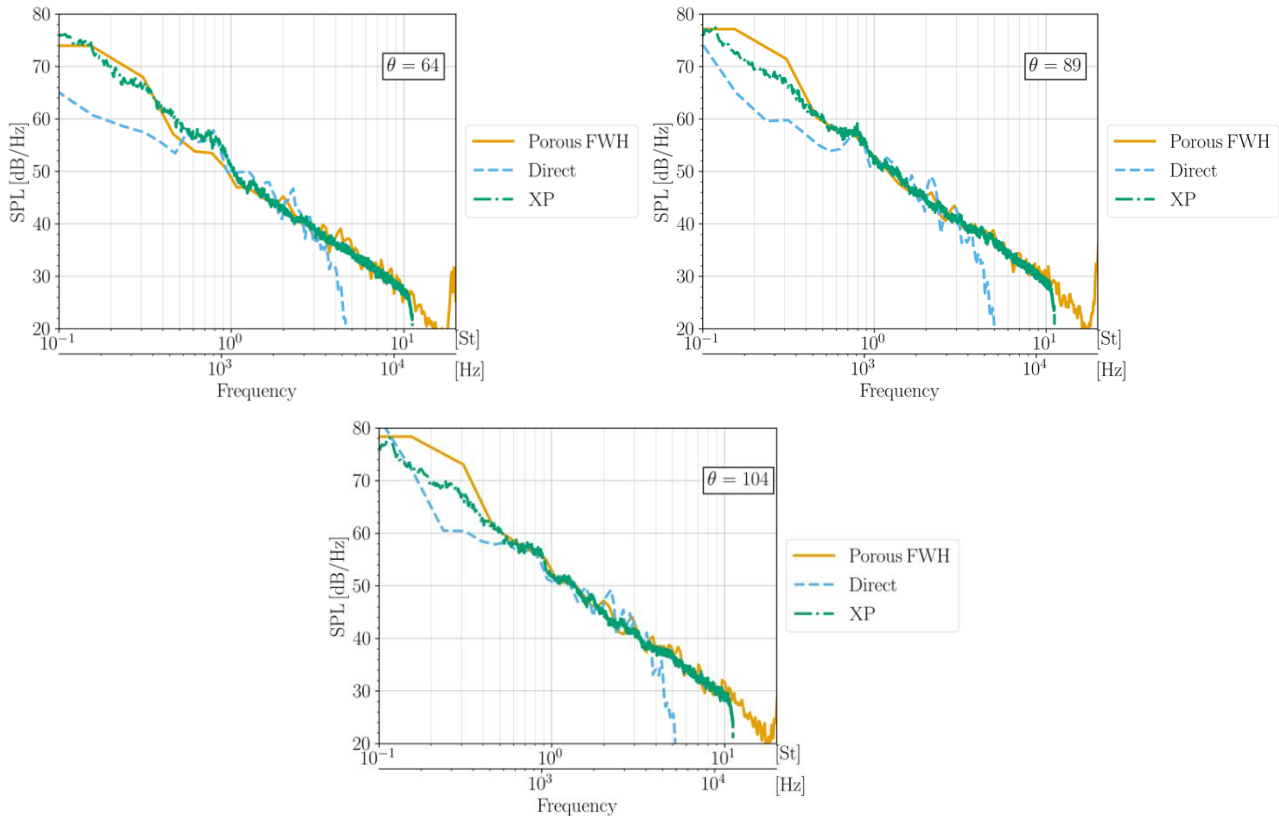


Figure 7.15: SPL spectra, acquired from flyover microphones (direct) at different angles and from FWH surfaces. XP stands for experimental data.

7.4 Yawed Case

To assess the impact of wing sweep on the effective change in the noise abatement by the deflected spoiler, a yawed configuration was studied. The spoiler was yawed by $\psi = 10^\circ$ along the symmetry plane at $\gamma = 0$ m. To assess the effective change due to the induced yaw effect, the spoiler was deflected at an angle of 30° , in comparison to the baseline validation configuration. Figure 7.16 shows a comparison of the far-field acoustics conducted by comparing the narrowband spectra for the wall-mounted spoiler for three polar locations along the overhead flyover arc at a polar angle of: (a) Forward arc at a polar angle $\theta = 76.25^\circ$, (b) overhead on top of the leading edge of the spoiler at a polar angle of $\theta = 89.97^\circ$, and (c) along the rearward arc downstream of the spoiler at a polar angle of $\theta = 101.5^\circ$.

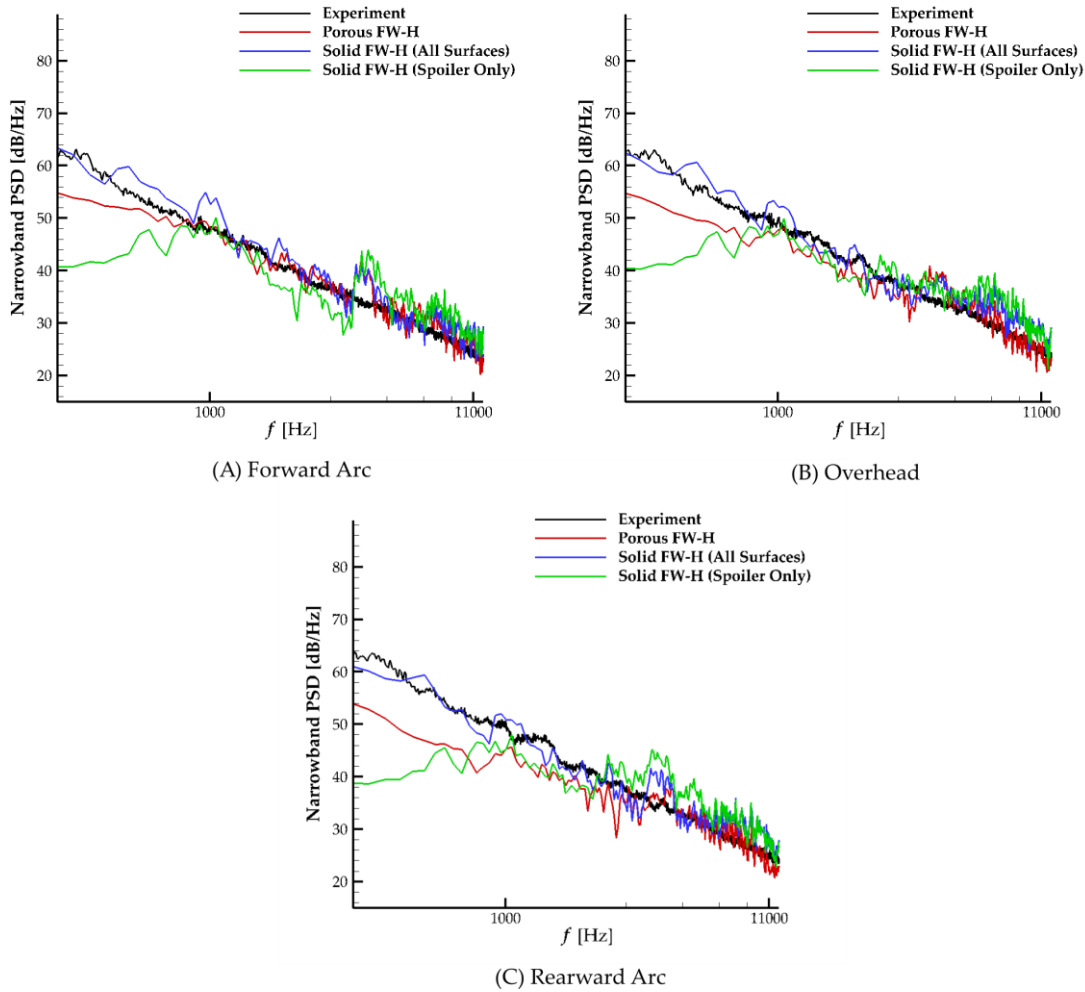


Figure 7.16: Comparison of the narrowband acoustic far-field for the wall-mounted spoiler deflected at a deflection angle of 90° along 3 overhead locations: (a) Forward arc upstream of spoiler, (b) Directly Overhead, (c) Rearward Arc downstream of the spoiler.

Similar to what was observed for the baseline case, agreement between the numerical far-field results and the experimental results were obtained between the narrowband frequency of 1 kHz and 3 kHz. Best agreement for all the flyover polar angles tested was obtained by using the solid FW-H surface for frequencies above 1 kHz where the contribution from the noise of the spoiler is not masked by the noise radiating from the endplate. The porous FW-H was observed to under predict the noise at low frequencies, below 1 kHz, which is a result of the noise contribution of the endplate. Similarly to previously analysed results, a broadband hump is observed at 4 kHz due to the interaction of the flow emanating through the hinge gap and the surface cavity formed during meshing of two surfaces at close proximity.

To assess the effective change in the noise radiated to the far field as a function of the yaw angle, a comparison of the ΔSPL_{yaw} between the one-third octave spectra for the yawed configuration and the baseline validation configuration was done as shown in Equation 5. The spectra were calculated using the solid FW-H surface given that it showed best agreement to the experimental results.

$$\Delta SPL_{yaw} = SPL_{yaw} - SPL_{validation} \quad \text{Eq.5}$$

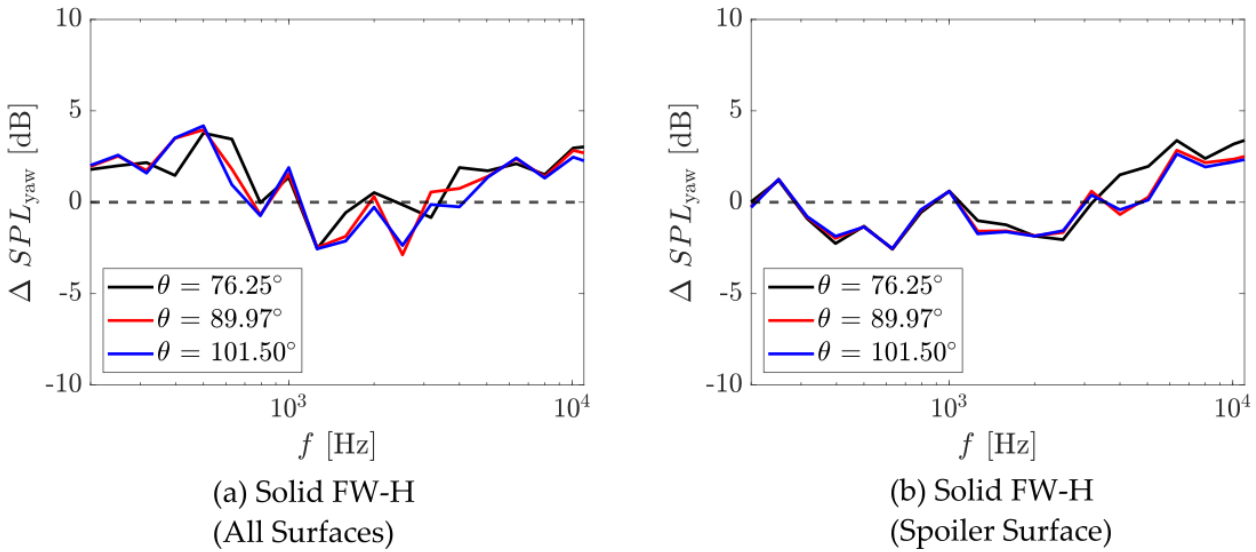


Figure 7.17: Comparison of the delta SPL between the yawed spoiler configuration and the baseline validation configuration for a spoiler deflection angle of 30°: (a) Contribution from all the solid surfaces, (b) Contribution of only the spoiler surface.

Previous results analysed for the spoiler deflected at 30°, have shown that the low frequency is dominated by the noise contribution radiating from the endplate. The spoiler contribution becomes significant beyond a narrowband frequency of 1 kHz. To ensure that the trailing edge of the endplate is parallel to the trailing edge of the yawed spoiler, a different endplate was used which had a larger surface area when compared to the baseline plate. To detach the contribution of the noise from the endplate from the noise generated by the flow topology due to a yawed spoiler, two different analysis were done. Figure 7.17(a) provides the ΔSPL_{yaw} comparison as a function of the contributions of all the model (including the endplate and the deflected spoiler), whilst Figure 7.17(b) provides the ΔSPL_{yaw} as a function of the contribution of the spoiler surface alone.

Results show that the effective change in the far-field noise due to yawing the spoiler varies as a function of frequency. When considering the changes only due to the contribution of the spoiler, shown in Figure 7.17(b), suppression in the overall noise levels was observed for most frequency regions below 3 kHz. At low frequencies below 1 kHz, a reduction of 2 dB is observed between 250 Hz and 1 kHz. An increase in the noise levels was observed at 250 Hz by 1.2 dB and at a frequency of 1 kHz by 0.6 dB. For the mid-frequency, noise suppression of 1.3 dB was observed up until a frequency of 3.17 kHz, after which a noise increase of up to 2 dB was achieved.

When including the endplate, an increase in the ΔSPL_{yaw} at low frequencies below 1 kHz was observed, confirming that at low frequencies, the noise contribution from the larger area of the yawed endplate impacts the results compared to the baseline results.

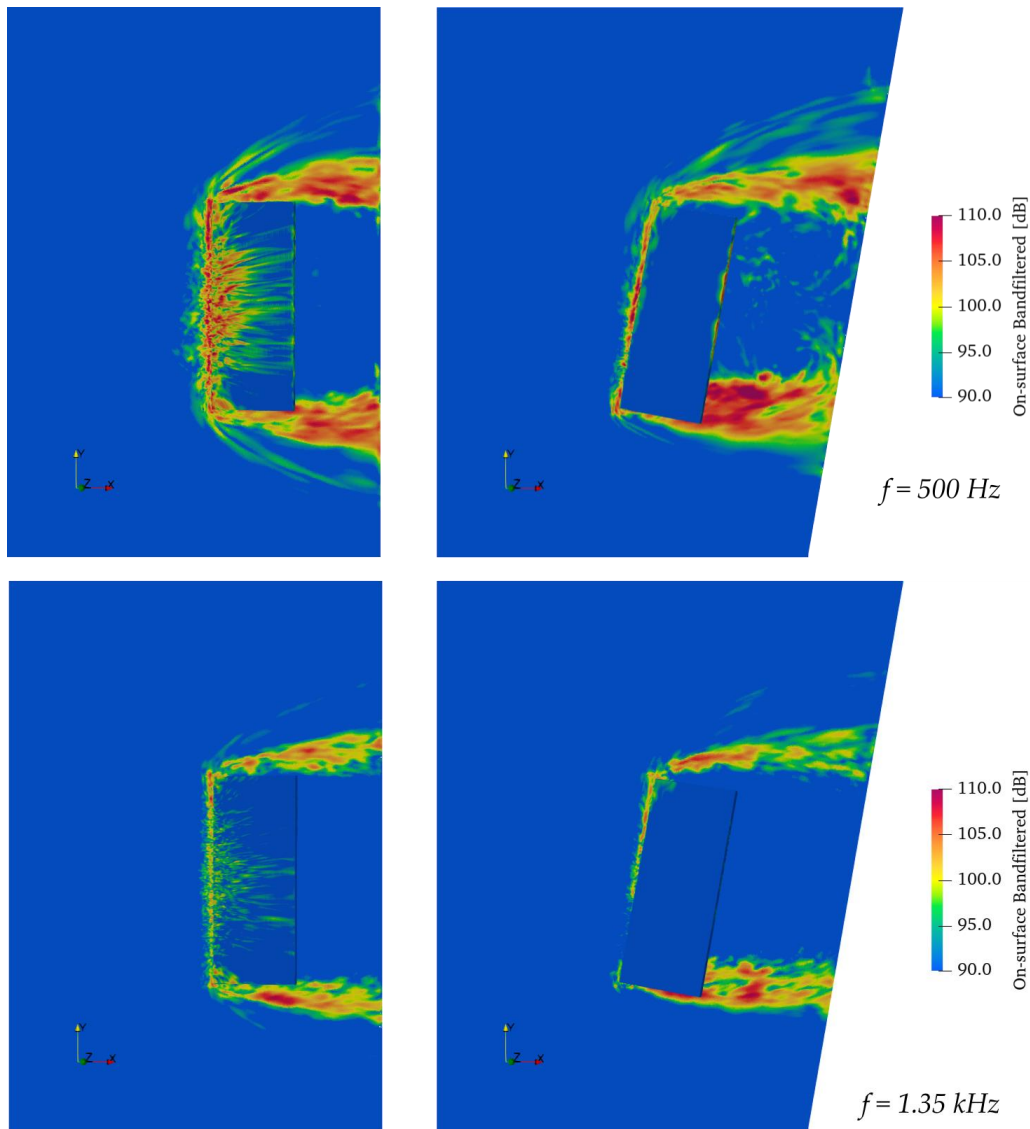


Figure 7.18: On-surface band filtered narrowband frequency between the baseline configuration and the yawed configuration for a spoiler deflected at 30° at a frequency of (a) $f = 500 \text{ Hz}$ and (b) $f = 1.35 \text{ kHz}$.

Figure 7.18 compares the on-surface band filtered narrowband frequency analysis for the baseline and the yawed configuration at a spoiler deflection angle of 30° . The analysis was done at two narrowband frequency of 500 Hz and 1.35 kHz. These frequencies correspond to instances in which the yawed configuration was found to be less noisy than the baseline configuration for the same deflection angle. The on-surface maps highlight that for the baseline configuration, a larger region of unsteady fluctuations forms upstream of the spoiler due to the upstream separation vortex. This, said, although upstream separation is also observed for the yawed configuration, as shown in Figure 7.19, the crosswind components of the flow along the yawed angle of the spoiler limits the growth of the horseshoe vortex, resulting in a region of lower fluctuations along the upstream face of the spoiler, and noise radiation to the far-field.

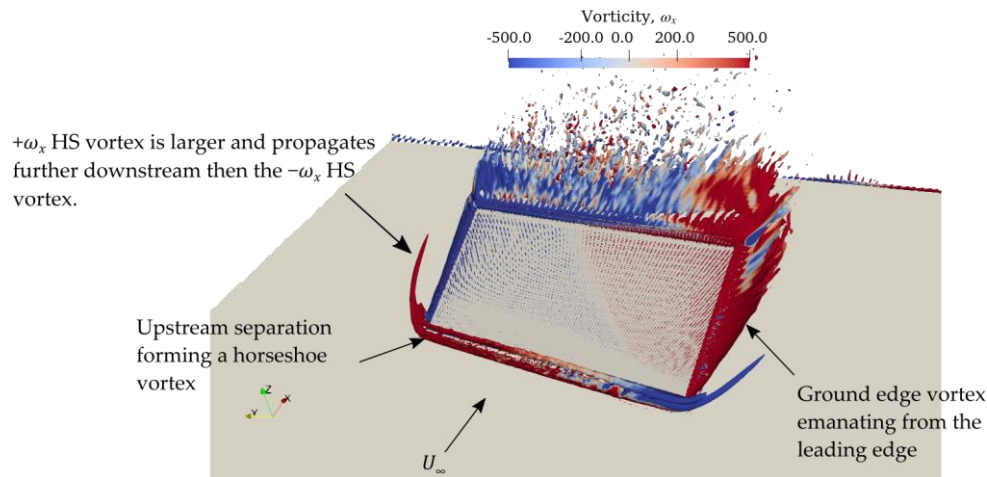


Figure 7.19: Q-criterion for the yawed spoiler configuration at a spoiler deflection angle of 30°.

Figure 7.19 highlights the flow topology for the yawed configuration. When compared to the baseline configurations, the upstream separation forming the horseshoe vortex is observed to convect further downstream along the positive vorticity leg when compared to the negative vorticity leg. This is because the saddle point of the upstream separation is along the windward side of the spoiler ($-y$) and hence the positive vorticity leg of the horse shoe vortex has more time to develop when compared to the opposite vorticity leg.

7.5 Side-by-Side (Simultaneous Deflection)

As depicted in Figure 7.20, for the simultaneous deflection case, the results from two distinct acoustic measurements techniques exhibit good agreement with experimental data within the frequency range of 4 to 10 Strouhal numbers. At lower Strouhal numbers, both microphones and FWH surface data show relatively little dependence on azimuthal angles. For Strouhal numbers greater than 10, the cutoff frequency in the direct acquisition spectra is nearly unaffected by the azimuthal angle, and a similar trend is observed for the FWH surfaces spectra. In contrast to the extended case, in this scenario, the peak of the porous FWH surfaces data at the highest Strouhal numbers gradually smears out with increasing directivity angle.

7.6 Side-by-Side (Spilt Angles)

As shown in Figure 7.21, no significant differences are apparent between the simulations of the current case and the previously presented cases. This is justifiable given the close-to-negligible relative differences found among the experimental data cases, as illustrated in Figure 7.22. The largest deviations, up to 2 dB/Hz, are observed between the SSI case and the others, indicating a noise increase from $St = 1$ onwards. This could be attributed to the simulation being designed to capture acoustics only up to $St = 1$, potentially leading to an overestimation of both FWH and direct propagation spectra at higher frequencies.

The misprediction of direct propagation spectra is likely a consequence of numerical and unphysical sources in the simulation, triggered by a poor resolution between the two spoilers; this issue is expected to be rectified by employing finer meshes.

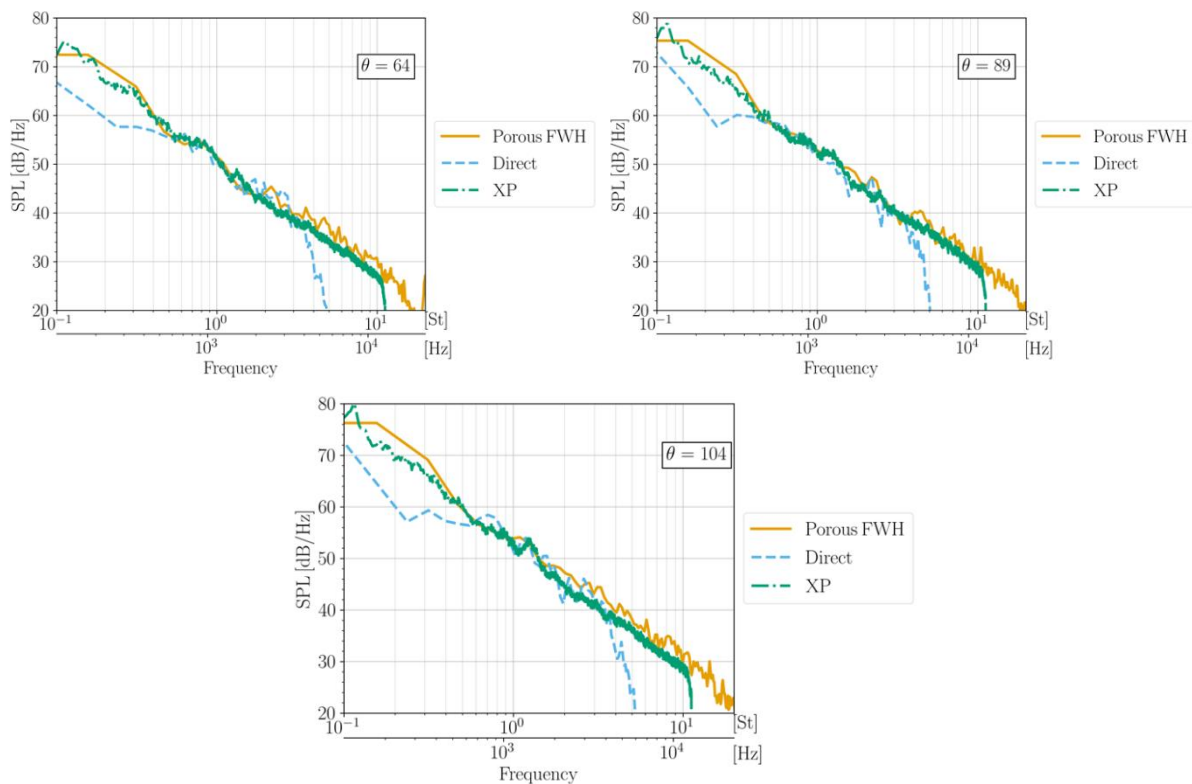


Figure 7.20: SPL spectra, acquired from flyover microphones (direct) at different angles and from FWH surfaces. XP stands for experimental data.

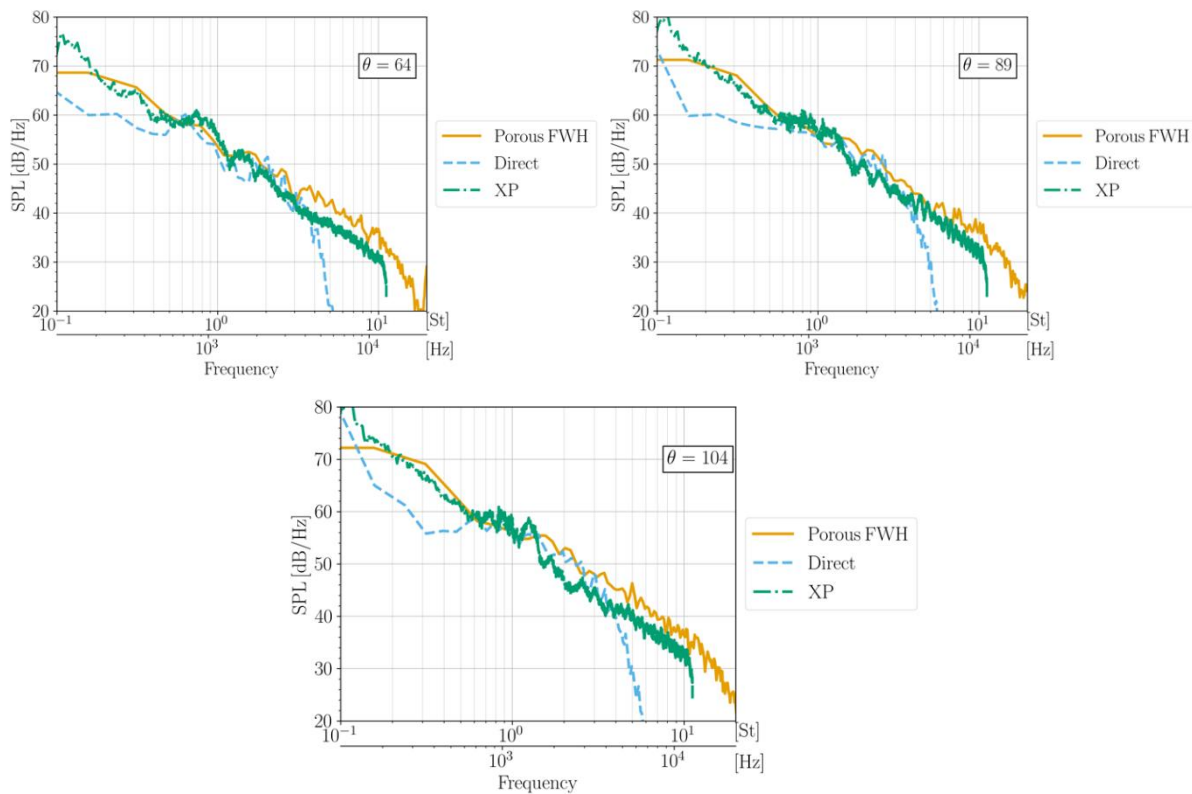


Figure 7.21: SPL spectra, acquired from flyover microphones (direct) at different angles and from FWH surfaces. XP stands for experimental data.

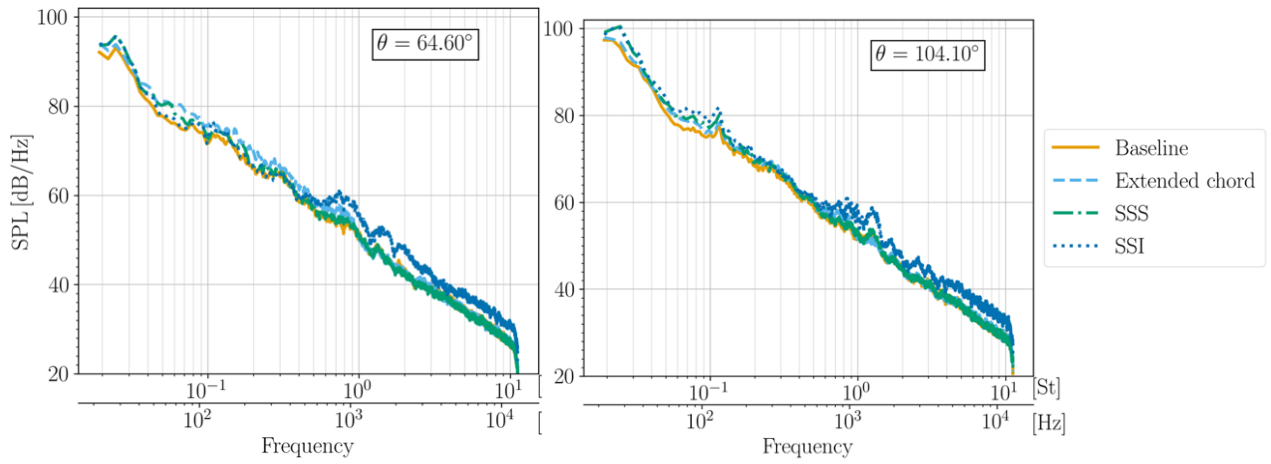


Figure 7.22: SPL spectra, acquired from flyover microphones (direct) at different angles and from FWH surfaces. Experimental data only.

8. Summary

In this deliverable, a numerical investigation of spoiler noise was performed in various configurations. Firstly, an experimental validation database for a spoiler mounted to a flat plate was described, which was a crucial part of the work performed in Task 4.4. The experimental database consisted of forces, on-surface pressure measurements, hotwire measurements, and particle image velocimetry measurements. The motivation behind mounting the spoiler to a flat plate was to decouple its sources from changes in the other high-lift wing sources when the spoiler is deflected. The spoiler was deflected at an angle of 30° for the validation case.

Results from the baseline numerical simulations, performed using the Lattice Boltzmann code ProLB, were compared to the experimental validation database for this case. In spite of the relatively simple geometries involved in this test case, it was still quite a challenging case to correctly simulate. In particular the upstream separation bubble, which ultimately formed the horseshoe vortex around the spoiler, was difficult to predict in the correct location upstream of the spoiler hinge line. Both UoS and CERFACS had a different approach to try and predict the correct boundary layer upstream of the hinge line. In the UoS simulations, the wall cell size was varied until the wall function gave the best prediction of the boundary layer thickness. CERFACS used mechanical forcing tailored to flow properties to force a turbulent boundary layer.

The on-surface pressure distributions showed that the base pressure on the downstream face of the spoiler was well predicted, the small discrepancies in the upstream separation bubble location and subsequent reattachment, resulted in small differences in the pressures on the upstream face of the spoiler.

The wake characteristics, mean velocities, and turbulent intensities, were determined from hotwire anemometry and particle image velocity. The numerical simulation showed good agreement with the experimental data. There was some difference in the interaction with the wake of the spoiler and the quiescent flow underneath the base plate, resulting in a slight overestimation of the base recirculation region. This led to a slightly larger wake in the numerical simulations. Also, the turbulent spectra showed a slight underprediction at low frequencies resulting in a slight underprediction in the turbulent intensity measured in the wake.

Reasonable agreement is observed between spectra computed from flyover microphones data and those from both direct and porous FWH propagations. CERFACS noted that data from solid FWH surfaces did not yield to reasonable agreements with flyover microphones' data. The UoS simulations also showed excellent agreement above 630 Hz with the porous FWH prediction. However, the solid FWH provided a better prediction at low frequencies as these frequencies were dominated by the pressure fluctuations on the mounting base plate, caused by the spoiler wake.

Using the validated numerical results, the flow topology of the deflected spoiler was described. It consisted of three main flow features. The first was a separation bubble upstream of the spoiler hinge resulting in a horseshoe vortex that wrapped around the sides of the spoiler. The second was ground edge vortices which were attached to the base plate up to the trailing-edge. These ground edge vortices rotated in the opposite sense to the horseshoe vortex on each side. The third was an arch-

type broadband wake downstream of the spoiler that was symmetric about the center span of the spoiler. The wake was characterised by an absence of coherent vortex shedding due to the mounting plate inhibiting the formation of a shear layer of opposite sign vorticity on the lower edge of the plate. The highest on-surface pressure fluctuations were close to the spoiler side edges. The acoustic source associated with the ground edge vortices and the spoiler side-edges were the dominant acoustic sources in this configuration, particularly as the frequency increased.

The effect of reducing the spoiler angle to 10° was to weaken the horseshow vortex. Also, the edge vortices stayed attached to the spoiler side edges for longer than at higher deflection angles. There was a strong broadband hump associated with flow through the spoiler gap at the hinge line. In terms of spoiler noise mitigation, this gap noise was identified as a potential source to be removed.

Increasing the deflection angle to 90° showed the separation point moved upstream of the spoiler. This resulted in a much stronger horseshoe vortex. The main acoustic source was as it rolled up around the edges of the spoiler. The results showed that the exact dominant mechanism depended on the deflection angle. Again, for this case, the hinge gap was a source of noise.

When the spoiler was yawed, there was a clear asymmetry between both edges. In general, there was an increase in noise at both low and high frequencies. The ground edge vortex was a stronger acoustic source on the side yawed into the wind. In terms of increasing chord and span there were only weak effects on the overall broadband noise. In order to mitigate the noise the spoiler gap should be closed and the horseshoe vortex should be weaken (typically by decreasing the spoiler angle). The acoustic sources associated with the side edge vortices are important and can be mitigated using typical methods used to reduce flap side edge vortices.

9. References

- Afzal, N. (1996). Wake Layer in a Turbulent Boundary Layer with Pressure Gradient: A New Approach. 95-118.
- Bruun, H. (1995). *Hot-wire Anemometry: Principles and Signal Analysis*. New Yoek: Oxford University Press.
- C Tropea, A. Y. (2007). Springer Handbook of Experimental Fluid Mechanics. Berlin: Springer.
- Dobrzynski, W. (2008). Almost 40 Years of Airframe Noise Research - What did we achieve? *14th Aeroacoustic Conference*. Vancouver: AIAA.
- H Sakamoto, M. A. (1983). Flow Around a Normal Plate of Finite Width Immersed in a Turebulent Boundary Layer. *Journal of Fluids Engineering*, 98-104.
- H. Sakamoto, H. H. (1986). Arch-Type Vortex Formed Behind a Normal Plate Placed in a Laminar Boudnar Layer. *Bulletin of JSME*, 2857-2862.
- Jorgensen, F. (1971). Directional Sensitivity of wire and fibre-film probes. DISA Information No.11.
- Jorgenson, F. (2002). How to measure turbulence with hot wire anemometers - a practical guide. Skovlunde: Dantec Dynamics A/S.
- Leveque, E., Touil, H., Malik, S., Ricot, D., & Sengissen, A. (2018). Wall-modeled large-eddy simulation of the flow past a rod-airfoil tandem by the Lattice Boltzmann method. *International Journal of Numerical Methods for Heat and Fluid Flow*, 1096-1116.